# OBSERVATIONS OF ATMOSPHERIC TURBULENCE DURING A LOW INTENSITY SURFACE FIRE

By

Joseph Patrick-Thayer Seitz

# **A THESIS**

Submitted to
Michigan State University
in partial fulfillment of the requirements
for the degree of

Geography—Master of Science

2022

#### **ABSTRACT**

# OBSERVATIONS OF ATMOSPHERIC TURBULENCE DURING A LOW INTENSITY SURFACE FIRE

By

# Joseph Patrick-Thayer Seitz

Ambient atmospheric environment affects the growth and spread of wildland fires, whereas heat and moisture release from the fires and the reduction of the surface drag in the burned areas can significantly alter local atmospheric conditions. Previous studies have investigated this interaction between the fire and the surrounding atmosphere, but the majority of these experiments were limited in horizontal density of observations and occur on large burn plot areas larger than several thousand square meters (more than a few acres). This study reports results from a densely instrumented prescribed surface burn of a plot size approximately one hundred square meters (10 m by 10 m) with a pine needle fuel loading of 0.5 kg m<sup>-2</sup>, a fuel moisture of 5.5%, and an ambient wind speed of about 2 m s<sup>-1</sup> (measured at 2.5 m). The analysis of the 10-Hz velocity and temperature data from the 16 sonic anemometers focuses on fireinduced atmospheric turbulence. By comparing the observations collected before, during and after the fire, the study displays how the fire can alter the heat and momentum exchanges between the combustion zone and the atmosphere above. Even for a plot as small as this, the perturbations of the fire to the ambient atmosphere depends strongly on the downwind distance from the initial fire line and the specific position relative to the fire front, revealing the existence of substantial heterogeneity across the plot. The results also have important implications for modeling smoke dispersion, as atmospheric dispersion characteristics in the vicinity of wildland fires are directly affected by fire-induced turbulence, showing a need for 1-2m grid spacing in fire behavior models to properly resolve atmosphere interactions relevant to turbulence.

#### **ACKNOWLEDGMENTS**

I would like to thank my co-advisors and committee members Dr. Joseph J. Charney, Dr. Shiyuan Zhong, and Dr. Julie Winkler for their support throughout my graduate degree in both coursework and becoming a better scientist. I would also like to thank the other scientists at that work in the fire group at the Forest Service Northern Research Station for creating an environment accommodating the growth of scientific curiosity, with significant appreciation for Dr. Warren Heilman who provided significant insights throughout the analyses of this study.

I would like to thank the financial support from the project 'Multi-scale Analyses of Wildland Fire Combustion Processes in Open canopied Forests using Coupled and Iteratively Informed Laboratory-, Field-, and Model-based Approaches' funded by the Department of Defense's Strategic Environmental Research and Development Program (SERDP) project, (Skowronski, PI) and the field team of the project that made the data available. I would also like to thank the Michigan State University Department of Geography, Environment, and Spatial Sciences for providing graduate teaching positions that allowed me to grow my teaching abilities and provided addition financial support during my graduate career.

Last but not least, I would like to thank my family and friends, especially my mother who was instrumental in creating a fascination in the physical sciences while also supporting me and being my number one fan throughout my entire life and career.

# TABLE OF CONTENTS

LIST OF FIGURES	V
CHAPTER I – INTRODUCTION	1
1.1 Overview	
1.2 Field Observations of Atmospheric Turbulence Associated with	
Wildland Fires	
1.3 Study Objectives	
·	
CHAPTER II – METHODS	
2.1 Experimental Set Up	
2.2 Data Processing	14
2.3 Case Description	15
2.3.1 Atmospheric Conditions	16
2.3.2 Fuel and Fire Spread	
2.4 Analysis Method	
CHAPTER III - RESULTS AND DISCUSSION	25
3.1 Fire-Induced Perturbations of Wind and Temperature	
3.2 Intensity of Fire-Induced Turbulence	
3.3 Fire-Induced Shear Stress	
3.4 Fire-Induced Turbulent Heat Flux	
3.5 Quadrant Analysis of Fire-Induce Turbulent Heat and	
Momentum Fluxes	38
CHAPTER IV – CONCLUSION AND FUTURE WORK	50
WORKS CITED	55

# LIST OF FIGURES

Figure 1. Sketch of the burn plot and the instruments deployed to the plot. The four capital letters (A, B, C and D) denote the four trusses and the four numbers (1, 2, 3, 4) refer to the 3D sonic anemometers on the trusses. Posts hanging on trusses B and C show the heights and location of thermocouples. The center post indicates the position of the infrared camera. The boxes next to the sonic anemometers indicate the radiometer/spectral camera pairs. The rectangular box on the ground indicates fuel cells for fuel loading estimation. The symbol near B2 indicates the TACO for emission data collection.
Figure 2. Surface meteorological condition on May 20, 2019, the day of burn No. 20, observed by the ASOS station at the McGuire U.S. Air Force Base in Burlington County, New Jersey approximately 11 km north of the burn site
Figure 3. Infrared images taken at 10 m above the center of the plot showing fuel bed temperature before, at and after ignition. Times are in LST
Figure 4. Time series of 10-Hz observations of temperature (T), horizontal wind speed (S) and vertical wind speed (w) observed by the 16 sonic anemometers
Figure 5. The number of sonic anemometers that recorded temperatures at or above a given threshold value (left) and the length of period over which the threshold was reached or exceeded (right)
Figure 6. Average wind direction during the pre-burn period for each of the 16 sonic anemometers (dots). The light blue dashed line indicates the average across all 16 sonic anemometers and the orange dashed line denotes the median
Figure 7. Illustration of sweep-ejection analysis for heat flux (left) and momentum flux (right)
Figure 8. Time series of 10 Hz streamwise (u, blue) and cross-stream (v, green) wind components, and 10 Hz temperature perturbations (T', red) recorded by each sonic anemometer at 2.5 m above the ground. The vertical dashed black lines indicate the burn period determined by the first and last occurrence of when T' is larger than 8 times the standard deviation. Time is the minutes since the start of the pre-burn period
Figure 9. Distributions of 10 Hz streamwise (u), cross-stream (v), and vertical (w) wind components, and temperature perturbations (T') during pre-burn, burn and post-burn periods. The box represents the 25th and 75th percentile of the data, with data inside the whiskers representing 99.3% of the data. The orange line in the boxes is the median value, the green triangle is the mean, and the blue shading is the density of values
Figure 10. 1-minute averaged turbulent kinetic energy (TKE) (red line) and the three components that make up the TKE for each sonic anemometer. The u component $(u'^2/2)$ , v component $(v'^2/2)$ , and w component $(w'^2/2)$ are notated as yellow, blue, and dark green, respectively29

Figure 11. Boxplot distributions of turbulent kinetic energy (TKE) and the velocity variance components (u'2/2, v'2/2 and w'2/2) during the pre-burn, burn and post-burn periods. The blue shading indicates the distribution, green diamond is the mean value, and orange line is the
median30
Figure 12. Time series of 1-minute averaged kinematic momentum flux $(u_*^2)$ and its u- and v-components $(u'w')$ and $v'w'$ , separated by sonic anemometer. Yellow circles indicate $u'w'$ , blue diamonds indicate $v'w'$ , and pink plusses indicate $u_*^2$
Figure 13. Boxplot distributions of friction velocity $(u_*^2)$ and its components $(\overline{u'w'})$ and $\overline{v'w'}$ and $\overline{v'w'}$ during the pre-burn, burn, and post-burn periods. The blue shading indicates the distribution, green diamond is the mean value, and orange line is the median
Figure 14. Time series of 1-minute averaged heat flux for each sonic anemometer and an overall distribution of values for all the sonic anemometers. Dark green dots on the 4x4 grid indicate the average heat flux value for each minute. The right panel shows the distribution of the heat flux for the entire burn plot in the pre-burn, burn, and post-burn periods
Figure 15. Quadrant analysis of the turbulent heat flux showing instantaneous outward interaction (green), ejection (red), inward interaction (blue), and sweep (orange) events at each of the 16 sonic anemometers, separated by burn period. The top row is the total magnitude of the 10Hz observations for the corresponding $T'w'$ perturbations in each period with the total heat flux value represented as a black diamond. The bottom row is the percentage of events occurring at each sonic separated by burn period. The sonic anemometers are arranged from west to east roughly following the fire spread under the fire plot.
Figure 16. Quadrant analysis of turbulent heat flux events for all sonic anemometers using instantaneous outward interaction (green), ejection (red), inward interaction (blue), and sweep (orange) for each period. The left plot is the summation of the magnitude of events of combined sonic anemometers before, during, and after the burn period. The right plot is the percentage of the type of events before, during, and after the burn
Figure 17. Quadrant analysis of the turbulent kinematic horizontal momentum flux showing instantaneous outward interaction (red), sweep (green), inward interaction (orange), and ejection (blue) events at each of the 16 sonic anemometers, separated by burn period. The top row is the total magnitude of the 10Hz observations for the corresponding <i>S'w'</i> perturbations in each period with the total momentum flux value represented as a black diamond. The bottom row is the percentage of events occurring at each sonic separated by burn period. The sonic anemometers are arranged from west to east roughly following the fire spread under the fire plot
Figure 18. Quadrant analysis of kinematic momentum flux events for all sonic anemometers using instantaneous outward interaction (red), sweep (green), inward interaction (orange), and ejection (blue) for each period. The left plot is the summation of the magnitude of events of combined sonic anemometers before, during, and after the burn period. The right plot is the percentage of the type of events before, during, and after the burn

Figure 19. 1-minute averaged perturbations of vertical wind (w') in blue, horizontal wind spaces	peed
(S') in yellow, and temperature (T') in red. The burn period is represented by the two dark	green
dashed vertical lines	48

## **CHAPTER I - INTRODUCTION**

#### 1.1 Overview

Over the past several decades, wildfire seasons in many parts of the world, especially the western United States, have grown more devastating (Balch et al., 2017; Jain et al., 2017).

California, for example, experienced its three worst wildfire seasons in recorded history in the past five years (https://www.fire.ca.gov/stats-events/). Fueled by a historical drought and extreme heat, these recent California wildfire seasons started earlier, lasted longer and burned millions of acres across the state. In 2021 alone, more than 2.5 million acres were burned in California. Besides California, other western states such as Colorado and New Mexico also experienced their largest wildfires in recent years. The 2020 Cameron Peak wildfire, the largest in Colorado wildfire history, burned more than 200,000 acres and wildfires in northern New Mexico in spring 2022 burned more than 600,000 acres, making 2022 the worst fire season in the state's history. The impacts of wildfires range from loss of property and human life to changes in biodiversity, reductions in visibility, degradation of environmental quality (particularly air quality) and impairment of human health (Moreira and Russo, 2007; Spracklen et al., 2007; Gill et al., 2013; Moreno et al., 2013).

The increase in large wildfires in the United States in recent years has been attributed to global warming associated with the increase in the greenhouse gas emissions (Liu *et al.*, 2010; Abatzoglou and Williams, 2016; Virgilio *et al.*, 2019). As the warming trend continues, it is projected that large wildfires are likely to increase in frequency and intensity in most regions of the United States (Luo *et al.*, 2013; Tang *et al.*, 2015; Zhong *et al.*, 2021).

Wildfires are directly affected by atmospheric conditions. Large wildfires are often fueled by prolonged periods of little or no precipitation, high temperature and low humidity that dry out trees, grasses, shrubs and other types of fuels (Finney et al., 2015; Littell et al., 2016; Kitzberger et al., 2017). Once ignited, the behaviors of wildfires, characterized by burn intensity, ember production, spotting, fire whirls and rate of spread, are directly affected by local wind speed and direction. Fires tend to spread in the direction the wind blows, and the stronger the wind speed the faster the fire spreads (Clark et al., 1996). Fire spread dominated by wind is also known as "wind-driven" fire spread, in contrast to "plume-driven" fire spread dominated by the sensible heat released during the burn, which is largely determined by fuel type, loading and moisture content (Byram, 1954). In addition to wind, another important factor affecting fire behavior is atmospheric turbulence, defined as irregular microscale  $(10^{-2} - 10^3 \text{ m})$  air motions in the forms of eddies that are superimposed on mean atmospheric motions (Stull, 1988). Turbulent eddies affect fire behavior as well as the transfer of gaseous and particulate emissions from fires to the atmosphere (Clements et al., 2008; Skowronski and Hom, 2015; Viegas and Neto, 2015; Heilman, 2021). While atmospheric conditions directly affect wildfire behavior, wildfires also modify the surrounding atmospheric environment. These modifications occur primarily through heat and moisture release, which can lead to the formation of pyrocumulus clouds, and through other factors such as drag reduction, whirl production and more importantly, pollutant emissions (Kuwana et al., 2008; Potter, 2012)

The understanding of fire and atmosphere interactions date back to more than a century ago when Beals *et al.* (1914) published what was widely considered the first scientific study about the influence of weather on large fires. Numerous studies using field observations (e.g., Byram, 1940; van Wagner, 1979; Potter, 1996), laboratory experiments (e.g., Rothermel and

Anderson, 1966; Rothermel, 1972; Beer, 1993; Wolfe et al., 1991) and numerical modeling (e.g. Clark et al., 2004; Sullivan, 2009a, 2009b, 2009c; Mell et al., 2007, 2009; Linn and Conningham, 2005; Linn et al., 2020) have helped advance our knowledge of how the ambient atmospheric conditions, particularly the mean temperature, humidity, wind speed and wind direction, affect fire behavior and how fire-induced perturbations feed back to the mean atmospheric flows. In general, high mean temperature and low humidity have been linked to more wildfire activity and larger area burned, but the correlation or the strength of the relationship differs significantly across geographical regions, types of vegetation and seasons of the year (Potter, 1996, 2012). Mean wind, especially mean surface wind, has been identified as the key determinant in fire-atmosphere interactions, as wind directly affects fire behavior and the momentum and scalar exchanges (heat, moisture, CO and CO<sub>2</sub>, Particulate Matter or PM, etc.) between the atmosphere and the combustion zone (Potter, 2012). In general, higher mean surface wind speed is linked to a faster spread rate, more spotting and stronger atmosphere and combustion zone exchanges (Viegas and Neto, 1991; Beer, 1979). Fires, on the other hand, draw air into the combustion region, producing convergence/divergence flow and updrafts/downdrafts that can be 100 times stronger than the mean vertical motions in the ambient atmosphere (Clements et al., 2007).

Compared to investigations into the relationships between fire behavior and the mean properties of atmospheric flows in the region surrounding the fire, relatively fewer studies have documented the interactions between fires and the atmospheric turbulent flows that play a key role in exchanges of momentum and scalar variables between the combustion zone and the atmosphere above. This lack of attention is largely attributable to the lack of observational and numerical tools capable of directly resolving the interactions between fire and atmospheric

turbulent flows. Nevertheless, progress on this topic has been made since the beginning of the 21<sup>st</sup> century, thanks to advances in both in-situ measurements capable of measuring high frequency fluctuations in a harsh environment (e.g., Clements *et al.*, 2007, 2020), remote sensing technologies (e.g., Katurji *et al.*, 2021) and to the proliferation of computing power enabling fine-scale numerical modeling that can simulate atmospheric turbulence in the vicinity of fires.

Below is a brief review of existing literature on the interactions between fire behavior and atmospheric turbulence. The review focuses on field observations as they relate to the current study.

# 1.2 Field Observations of Atmospheric Turbulence Associated with Wildland Fires

Atmospheric turbulence refers to irregular microscale (10<sup>-2</sup> – 10<sup>3</sup> m) motions superimposed on mean atmospheric motions (Stull, 1988). Turbulence in the atmosphere is generated primarily by changes in wind speed and/or direction, known as mechanical turbulence, and by convection, referred to as thermal turbulence. Mechanical turbulence is often generated when air flow encounters surface drag, rough terrain or other natural or man-made obstacles and boundaries separating different air masses (e.g., weather fronts), different land cover types (e.g., grass vs. forested land) or land use types (e.g., agriculture vs. urban). Thermal turbulence is produced when heated surface air rises up in the atmosphere (convection), which commonly occurs during daytime when incoming solar radiation absorbed by the earth's surface exceeds outgoing terrestrial radiation. Fire-induced turbulence is a type of thermal turbulence in that heat released by combustion produces buoyant plumes that rise up from the combustion zone.

In-situ monitoring of fire behavior and fire-atmosphere interactions during wildland fires dates back to the 1990s. The International Crown Fire Modeling Experiment (ICFME) (Stocks et al. 2004), which was conducted over a forested plot dominated by jack pines and black spruce in Fort Providence, Northwest Territories, Canada, between 1995-2001, collected turbulence data using fast-response sonic anemometers located along the perimeter of burn plots. The data was used to document the generation of turbulent eddies by the fires and the influence of turbulent wind gusts on fire spread rates (Clark et al., 1999; Taylor et al., 2004). But not until the beginning of the 21<sup>st</sup> century were field campaigns able to collect systematic turbulence measurements inside active burn plots. Perhaps the first comprehensive field experiment where intensive turbulence data were collected during wildland fires was FireFlux, conducted on February 23, 2006, in Galveston, Texas (Clements et al., 2007; Clements et al., 2008). The experiment took place on a 155-acre plot of native tall-grass prairie and the fire was a winddriven or head fire. Fire-atmosphere interactions were monitored using a tall (43 m) and a short (10 m) instrumented micrometeorological flux tower within the burn plot, and background atmospheric conditions were documented using a surface weather station and a radiosonde station near the burn plot. Modifications to the ambient atmosphere by the grass fire were observed by 2 sodars and a tethered balloon sounding system located immediately downwind of the plot. Turbulent fluctuations, including fire-induced turbulence and its variations with height above the combustion layer, were collected using an array of fast response sonic anemometers mounted at multiple levels on the tall (2, 10, 28, 43 m) and the short (2.3 and 10 m) tower. Fast response moisture and CO<sub>2</sub> fluctuations were also measured using Open Path Gas Analyzers (at 10 and 28.5 m on the tall tower). The results revealed a dramatic increase in turbulence associated with the fire front. Specifically, turbulence intensity in the fire front was found to be

4-5 times greater than that of the ambient environment, with turbulence kinetic energy increasing from approximately 2 m<sup>2</sup>s<sup>-2</sup> before fire front passage to approximately 10 m<sup>2</sup>s<sup>-2</sup> during the fire front passage. Turbulent shear stress, measured by friction velocity, increased approximately 3 times to about 3 m s<sup>-1</sup> from that of the ambient value of slightly less than 1 m s<sup>-1</sup>. The maximum kinematic heat flux, which increased with height, reached 25 K m s<sup>-1</sup> (approximately 28 KW m<sup>-2</sup>) at the 43 m level (Clements *et al.*, 2008). The increase in turbulence energy was found to be due primarily to large eddies rather than small eddies.

A follow up field experiment, known as FireFlux-II, took place at the same site 7 years later, with more measurements designed to fill gaps in the original FireFlux experiment and provide further information on fire—atmosphere interactions and fire-induced turbulence regimes (Clements *et al.*, 2019). Important additions to the turbulence measurements included two 10 m towers in the burn plot and a 32-m mobile tower immediately downwind of the burn plot, bringing the total number of flux towers to five. Fast response sonic anemometers on these micrometeorological towers captured the spatial variations of fire-induced turbulence and the turbulence regimes associated with the flank fire, in addition to head fire. The data from FireFlux II have been used to validate fire behavior models, but the focus was on comparison of observed and modeled fire spread rates. Results on the intensive collection of turbulence data from FireFlux II are yet to be reported in peer-reviewed literature.

The data collected from FireFlux and FireFlux II experiments provided unprecedented direct turbulence measurements during intense grass fires. Another set of wildland fire experiments that took place in the New Jersey Pine Barrens, on the other hand, provided information on fire-induced turbulence during low-intensity forest understory fires (Heilman *et al.* 2015, 2017, 2019 and 2021). The first two experiments were conducted in March 2011 and

2012 as part of a research project under the auspices of the Joint Fire Science Program and the third experiment was carried out in February 2021 as part of a research project sponsored by the Strategic Environmental Research and Development Program (SERDP). The burn plots for these experiments, which were in the same areas of the Pine Barrens, were about 250 acres in size, with forest understory vegetation (average about 1 m height) composed of blueberry, huckleberry and scrub oak and overstory vegetation (average about 20 m height) composed of pitch pine and mixed oak. Deciduous vegetation in the burn plots had not leafed out during the burns. Turbulence data were collected using sonic anemometers and thermocouples mounted on 20-, 10- and 3-m flux towers within the burn plots, and the sampling rate for all three experiments was 10 Hz. In addition to the differences in fuel type (forest understory) between the FireFlux and Fire Flux II (grass fuel), the New Jersey Pine Barrens burns were backing fires that spread against background wind with spread rates less than 2 m min<sup>-1</sup>. This rate was more than 20 times slower than the spread rate of the grass fire in FireFlux and FireFlux II (about 40 m min<sup>-1</sup>) despite similar background wind speed (about 3 m s<sup>-1</sup>). Furthermore, these forest understory fires were low intensity fires (~50-300 kW m<sup>-2</sup>) while the grass fires were high intensity fires (~ 3000 kW m<sup>-2</sup>). Consequently, the increases in turbulence intensity, transport and mixing associated with surface fires were much smaller in these low-intensity forest understory fires than in the intense grass fires.

The data from these forest understory fire experiments revealed substantial differences in turbulence intensity, stress, and fluxes across the canopy layer, which complicated the evolution of local turbulence regimes and their interaction with spreading fires. Specifically, the data showed that fire-induced increases in turbulent kinetic energy are considerably larger near the top of the forest canopy layer than within the canopy, implying that vertical mixing or transport

of fire emissions (e.g., PM, moisture and heat) could be substantially larger near the canopy top than within the canopy layer (Heilman *et al.*, 2015). The observations also revealed that an anisotropic turbulence regime tends to persist throughout the vertical extent of overstory canopy layers, even in the highly buoyant plume during the passage of a fire front. The results suggested that spreading line fires can have a substantial effect on the skewness of daytime velocity distributions typically found inside forest vegetation layers, and that the contributions to turbulence production and evolution from mechanical shear production and diffusion can be very different in the pre-fire and post-fire environments (Heilman *et al.*, 2017).

The data from both the Texas grass fires and New Jersey forest understory fires have also provided insight into the turbulent momentum and heat transfer processes associated with eddy motions characterized by updrafts and downdrafts that are enhanced by fires. These fire-enhanced turbulence updrafts and downdrafts transfer warmer air (or lower momentum air) from the surface upward, a process known as "ejection" and colder air (or higher momentum air) downward to the surface, a process referred to as "sweep", which act to redistribute energy between the combustion layer and the atmosphere above (Heilman *et al.*, 2021). The analysis of the data suggests that wildland fires in grass or forest environments can substantially alter the relative importance of the sweep and ejection processes in redistributing momentum, energy and other species in the lower atmosphere (Heilman *et al.*, 2021). For turbulent momentum transfer, sweep events, or downward momentum transfer, were found to play a dominant role at the fire front (regardless of the fire types) despite the stronger updrafts than downdrafts at the front. However, the effect of fires on turbulent heat transfer is different between the heading grassfires and the backing forest understory fires. The former (grass, head fire) tends to be dominated by

ejection events while in the latter case (forest, backing fire), ejection and sweep events contribute comparably (Heilman *et al.*, 2021).

Both the Texas and New Jersey field experiments mentioned above were conducted over plots on relatively flat terrain. However, wildfire behaviors can be affected significantly by topography (Werth *et al.*, 2011; Sharples, 2009; and Sharples *et al.*, 2012). This is because topography exerts a strong influence on both weather and fuel conditions (Bennie *et al.*, 2008; Ebel, 2013; Billmire *et al.*, 2014; Calviño-Cancela *et al.*, 2017; Povak *et al.*, 2018) and consequently topography, along with weather and fuel, forms the fire behavior triangle (Countryman, 1972; Schmidt *et al.*, 2016). A series of prescribed burn experiments were conducted in complex terrain environments in California between 2008 and 2012. Three of these experiments were conducted in plots on simple sloping terrain (Seto and Clements *et al.*, 2011; Seto *et al.*, 2013; Clements and Seto, 2015; Amaya and Clements, 2020) and one was in a narrow valley (Seto and Clements, 2011). The sizes of burn plots in these experiments ranged from 5 acres to 35 acres, but all plots were dominated by grass fuels.

The grass fire on slope experiments included both heading (spreading with upslope winds) and backing (spreading against downslope wind) fires, and the grass fire in the valley experiment had mixed fire types, shifting from backing fire initially to heading fire later after a sea breeze arrived at the site. The observational platforms consisted of primarily in-situ micrometeorological towers, which were augmented by remote equipment such as sodar and Doppler Lidar. Data from these experiments provided unique information on the interactions between terrain-induced circulations and fire-induced flows. The results showed that terrain-induced slope flows and valley winds can interact with fire-induced flows to enhance horizontal and vertical wind shears that subsequently contribute to turbulence production. The interactions

of fire-induced flows with slope winds also produce local convergence or divergence with strong updrafts and downdrafts. Fire regimes tend to be anisotropic right above fire fronts, moving towards isotropic higher up (Seto *et al.*, 2013, Clements and Seto, 2015; Amaya and Clements, 2020). The data from these studies also revealed an increase in turbulent energy in both velocity and temperature spectra at higher frequencies, as fire fronts shed small eddies, and an increase at lower frequencies that are related to the strengths of the cross-stream wind component generated by the fire and enhanced by topography (Seto *et al.*, 2013).

A comprehensive review of studies on atmospheric turbulence in wildfire environments has been provided recently by Heilman (2021), which also discussed the implications of the findings to modeling fire behavior and smoke dispersion.

# 1.3 Study Objectives

Since all the field experiments mentioned above were conducted on burn plots that ranged from 5 to 100 acres, it was not feasible to cover the large burn plots with the few available towers. Therefore, the measurement strategy of these experiments focused on vertical variations of fire-atmosphere interactions and fire-induced turbulence using tall towers at a few key spots. Laboratory studies of fire-atmosphere interactions (see reviews by Forthofer and Goodrick, 2011), on the other hand, were limited to the small end of the burn scales (10<sup>0</sup> - 10<sup>1</sup> m on the side) and occurred under controlled conditions not representative of atmospheric environments in outdoor fires. There is a gap in the intermediate scale between the large-scale burns and the small-scale laboratory experiments. As part of the SERDP fire project discussed above, a series of intermediate-scale burns were conducted with a goal of filling in this scale gap

by quantifying the interactions among fuel-bed structure, moisture content, and meteorological factors (e.g., wind, humidity and temperature) driving variable fire behavior.

This study presents results from the analyses of turbulence data from one of these intermediate, fuel-bed scale burns. The results provide base knowledge about fire-induced turbulence during fuel-bed scale burns, bridging the gap in our knowledge about fire-atmosphere interactions between the management-scale and the laboratory-scale burns. The central question is: how does the fuel-bed scale surface fire modify atmospheric turbulence in the surface layer (lowest 10-100 m of the atmosphere)? Specifically, this study quantifies differences in turbulence intensity, turbulent shear stress or momentum flux, and turbulent heat flux before the fire is ignited, as the fire is spreading across the burn plot and after the fire exited the plot. In addition, the study sheds light on the specific processes contributing to the changes in momentum and heat transfer between the fuel-bed and the atmosphere above.

The experiment site and data as well as analysis method are described in Chapter 2 and the results are presented in Chapter 3. Chapter 4 provides a summary of the study, draws conclusions, and ends with future outlook, and finally works cited are listed in Chapter 5.

#### **CHAPTER II - METHODS**

# 2.1 Experimental Set Up

A series of 36 fuel-bed-scale burn experiments were conducted between March 2018 and June 2019 on 10 m x 10 m plots in a pitch pine plantation at the Silas Little Experimental Forest in New Lisbon, New Jersey. Of the 36 burns attempted, 5 included unsuccessful ignitions. Burns 1-10 were conducted on different burn plots on the Experimental Forest, whereas burns 11-36 were conducted on the same burn plot with burned fuels removed after each burn and replaced with new fuels.

Fuels for these burns consisted primarily of pitch pine needles and pine-oak foliage mixes. Target fresh (field) weight loadings for most burns, measured with a Pezola scale, averaged 480 g m<sup>-2</sup>, and for some burns the target loading was doubled to 960 g m<sup>-2</sup> or tripled to 1440 g m<sup>-2</sup>. The fuels were placed uniformly across the burn plot.

The measurement strategies were nearly identical for all the burns. Both remote sensing observations with a terrestrial scanning LiDAR (Faro Focus3D X330 HRD, Faro Technologies, Lake Mary, FL) and in-situ measurements known as destructive harvests were utilized to estimate fuel loading and moisture content before and fuel consumption after each burn. Infrared cameras, thermocouples and spectral sensors were used to measure flame position, gases, temperature, and radiant intensity. Atmospheric conditions, particularly turbulent fluxes, were measured by an array of three-dimensional (3D) ultrasonic anemometers (81000V, R. M. Young Inc.).

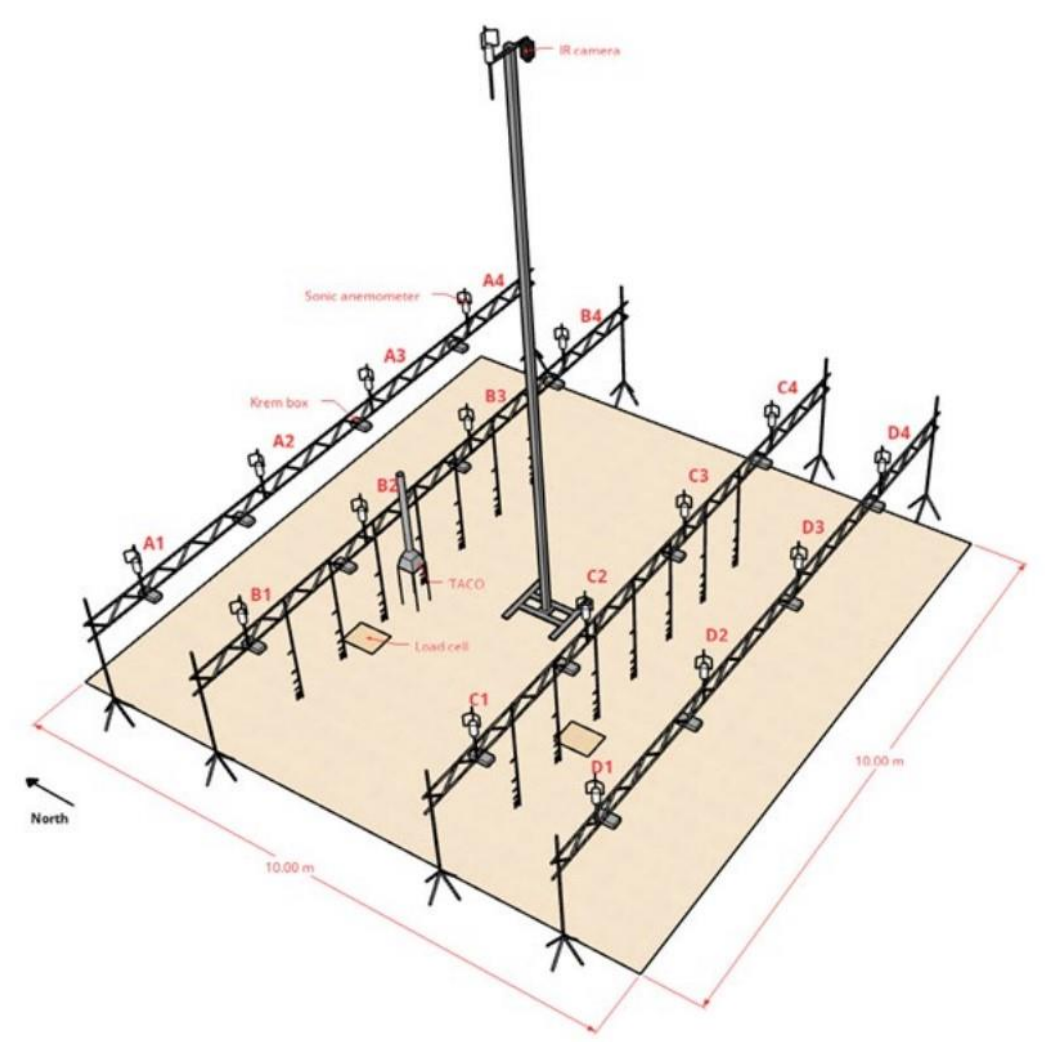


Figure 1. Sketch of the burn plot and the instruments deployed to the plot. The four capital letters (A, B, C and D) denote the four trusses and the four numbers (1, 2, 3, 4) refer to the 3D sonic anemometers on the trusses. Posts hanging on trusses B and C show the heights and location of thermocouples. The center post indicates the position of the infrared camera. The boxes next to the sonic anemometers indicate the radiometer/spectral camera pairs. The rectangular box on the ground indicates fuel cells for fuel loading estimation. The symbol near B2 indicates the TACO for emission data collection.

A typical 10 m x 10 m burn plot and the instrumentation are illustrated in Figure 1. The 10 m x 10 m plot was densely monitored by instruments mounted on four east-west-oriented trusses labeled A (northern most) to D (southernmost). On each truss, there were four 3D sonic anemometers labeled 1 to 4 from west to east. These sonic anemometers were mounted at 2.5m

or 3m above the ground level (AGL), depending on the burn, to collect u-, v-, and w-components of the wind and the temperature at a sampling rate of 10 Hz. Additional 10-Hz temperature data were also obtained using fine-wire thermocouples mounted at a range of heights (0, 5, 10, 20, 30, 50, 100 cm) mounted on the two inner trusses (B and C). A radiometer/visible spectrum camera pair (Kremens et al., 2012; Kremens et al., 2017) was mounted adjacent to each sonic anemometer to measure radiative heat fluxes and flame arrival times and persistence. Spatially explicit fire spread data were collected with an FLIR infrared video-camera (A655SC, FOL6 100.0-650.0 C lens, FLIR Systems Inc., Wilsonville, OR) mounted on top of a 10 m post in the center of the plot. For some burns, a field calorimetry hood (labeled TACO next to B2) with an inlet oriented over a portion of the fuel bed was used to sample O<sub>2</sub>, CO<sub>2</sub>, and CO concentrations in buoyant plumes. Gas concentrations were measured at 1 Hz using an Infrared gas analyzer (Crestline NDIR 7911, Crestline, Livermore, CA). Depending on ambient wind direction around the time of the burn, these fires could be either backing or head fires. For all the burns, a single 10-meter cord was soaked in accelerant, stretched across one end of the 10 m x 10 m plot, ignited and then dropped on the fuel bed to produce a near linear ignition.

## 2.2 Data Processing

Data from the 16 sonic anemometers and fine-wire thermocouples were logged at 10 Hz using Campbell Scientific CR3000 dataloggers. All the 10 Hz data underwent a quality assurance/control process to remove spurious values. The process first started with removing data that occurred before the first common timestamp recorded by each instrument in the instrument array. This provided a starting point for the observations for the burn period. Data from sonic anemometers (R. M. Young 18000V) include a self-reporting diagnostic column

where any non-zero number is considered an invalid measurement, so any measurement that reported a non-zero diagnostic code was removed. Following this initial step, data that fell outside RM Young 81000V sonic anemometer operating parameters (operational wind speed and temperatures are  $\pm 40$  m/s and  $\pm 50$  °C, respectively) were also removed.

The horizontal wind velocities were rotated into a streamwise coordinate system where the u-component becomes the streamwise component, defined by the prevailing wind direction, and the v-component becomes the cross-stream component, defined as perpendicular to the prevailing wind direction. Vertical winds were not corrected for tilt because of the short observational period (less than an hour) and because the burn plot was on level ground and each sonic anemometer was carefully mounted so that the wind sensors were very close to true horizontal and vertical planes. The results (presented below) indeed suggested that the contamination of vertical velocity by horizontal velocities were negligibly small as the average vertical wind speed during the pre-burn period was nearly zero. The sonic temperature was not corrected for humidity because the influence was thought to be small.

# 2.3 Case Description

The current study focuses on one specific burn case (burn No. 20) that occurred on May 20, 2019. This particular burn was chosen because the data was found to be cleaner (e.g. missing data points and data outside of the operational parameters of the sonic anemometers are comparatively uncommon) than most of the other burns, and the burn pattern represented a typical pattern of the burn series. Note that the sonic anemometers for burn No. 20 were mounted 2.5 m above the ground. In analyzing a single burn for this study, the goal is to establish a baseline case that could be used for comparisons with data from other burns to understand the

impact of different fuel conditions (types, loading, and moisture content) as well as different ambient atmospheric conditions (wind speed and direction, temperature and stability).

# 2.3.1 Atmospheric Conditions

On the day of the burn, the surface meteorological condition in the area is indicated by the data from the Automated Surface Observing System (ASOS) station located at the McGuire U.S. Air Force Base in Burlington County, New Jersey, approximately 11 km north of the experiment site (Figure 2). Ambient winds were south-southwesterly in the morning between 1 and 5 m s<sup>-1</sup>. Wind speeds increased near midday to 5-10 m s<sup>-1</sup> along with a direction shift from south-southwesterly to west-southwesterly. This wind speed increase was likely due to the mixing of higher winds from above to the surface as the mixing layer grew higher during the day. The growth of the mixing layer was a result of increased turbulent mixing associated with surface heating, as indicated by an increase in surface temperatures from about 20 °C in the morning to slightly above 30 °C around 1400 Local Standard Time (LST) and a corresponding

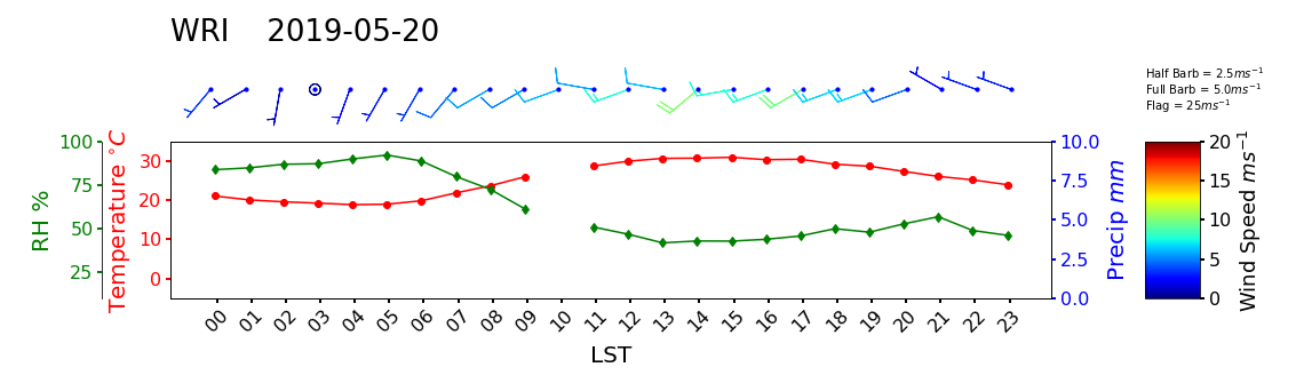


Figure 2. Surface meteorological condition on May 20, 2019, the day of burn No. 20, observed by the ASOS station at the McGuire U.S. Air Force Base in Burlington County, New Jersey approximately 11 km north of the burn site.

decrease in relative humidity from over 75% in the morning to less than 50% in the early afternoon.

# 2.3.2 Fuel and Fire Spread

The fuel for this burn was pine needles with a fuel mass about  $0.5 \text{ kg m}^{-2}$ , and fuel moisture content was about 5.5%. At the fuel bed level around the time of the burn, the average air temperature was about  $31.5 \, ^{\circ}\text{C}$ , wind speed was  $1.8 \, \text{m s}^{-1}$  and relative humidity was 39%.

The fire was ignited at around 14:25 LST with a 10-meter accelerant-soaked cord that stretched across the western boundary of the plot. A sequence of infrared images captures the changes in temperature from just before the ignition (upper-left image), to immediately after the

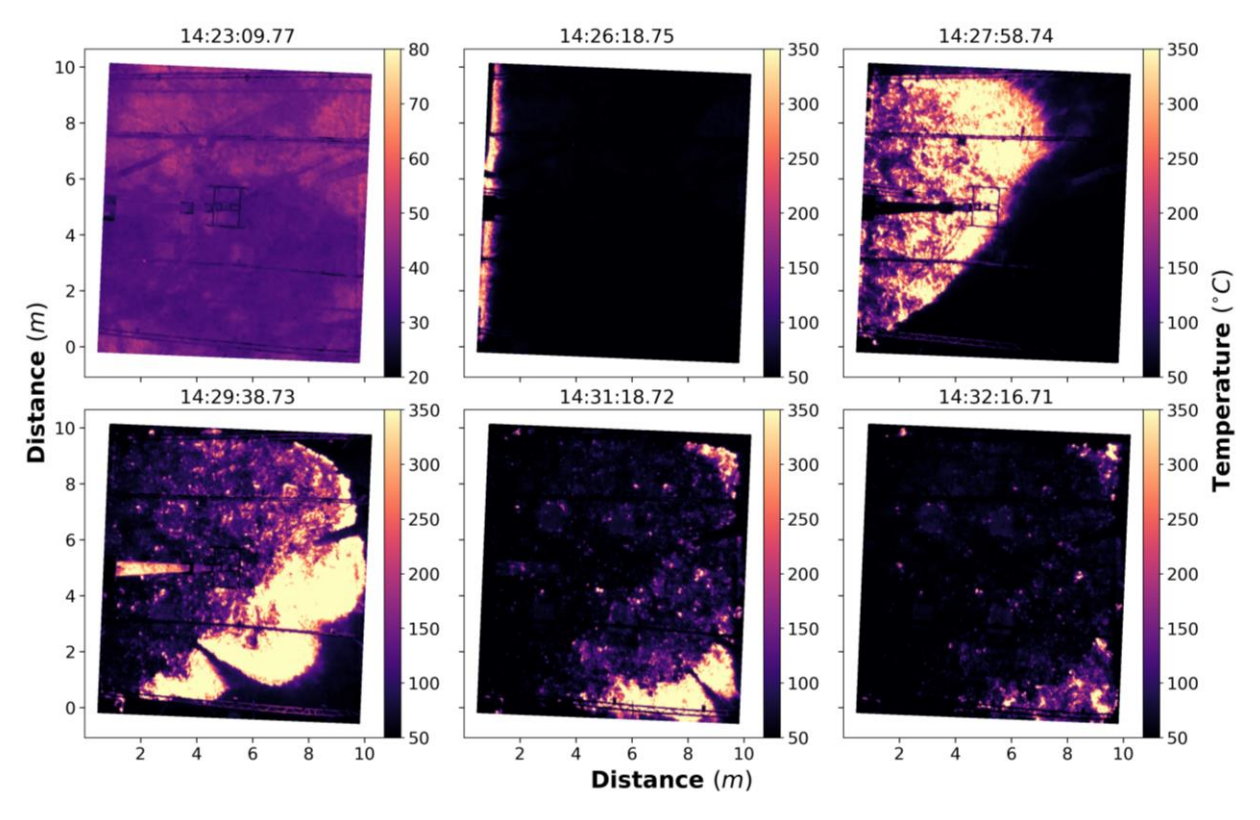


Figure 3. Infrared images taken at 10 m above the center of the plot showing fuel bed temperature before, at and after ignition. Times are in LST.

ignition (upper-center image), to minutes following the ignition as the fire spread across the plot (the rest of the images). Note that the pre-burn image uses a different color scheme to allow the visualization of the four trusses and the center post with the infrared camera. The second image, which corresponds to 14:26:18 LST (immediately after the ignition) clearly reveals that the ignition produced a line fire parallel to the western boundary of the plot. The following images show how the line fire spread in the direction of the west-southwesterly background wind towards the east-northeast over the next few minutes. The initial spread is faster on the northern portion of the domain, as expected from the south-southwesterly wind direction (upper-right image, corresponding to 14:27:58 LST). As the fire burns through the northern portion of the plot, the fire front catches up in the southern portion (lower left and center images taken at 14:29:38 and 14:31:18 LST, respectively). The fire ended at around 14:32:16 LST (lower right image) as the fire front reached the eastern boundary of the plot and ran out of fuel to continue. The average fire spread rate, estimated by the data from the infrared camera, is about 5.4 cm s<sup>-1</sup>.

## 2.4 Analysis Method

Atmospheric perturbations for the turbulence analysis are defined as the differences between the instantaneous observations and the mean values:

$$\phi' = \phi - \overline{\phi} \tag{1}$$

Where  $\overline{\varphi}$  is the mean value that is calculated by block-averages

$$\overline{\Phi} = \sum_{n=1}^{N} \Phi_n \tag{2}$$

where N is the number of samples over the averaging period or the time block and the mean values represent the mean state of the atmospheric flow. In traditional turbulence studies, mean state is usually determined using data over a period of a few minutes up to 1 hour, depending on atmospheric stability and the scale of interest. However, the block-averaged values during the period of fire are likely to be contaminated by the fire and therefore poorly represent the mean background flow in this (and many other) fire cases. To resolve this issue, Seto *et al.* (2013) and Heilman *et al.* (2021) propose that the block-averaged means for the fire period be replaced by block-averaged means calculated during the pre-burn period. In order to adopt this approach, the

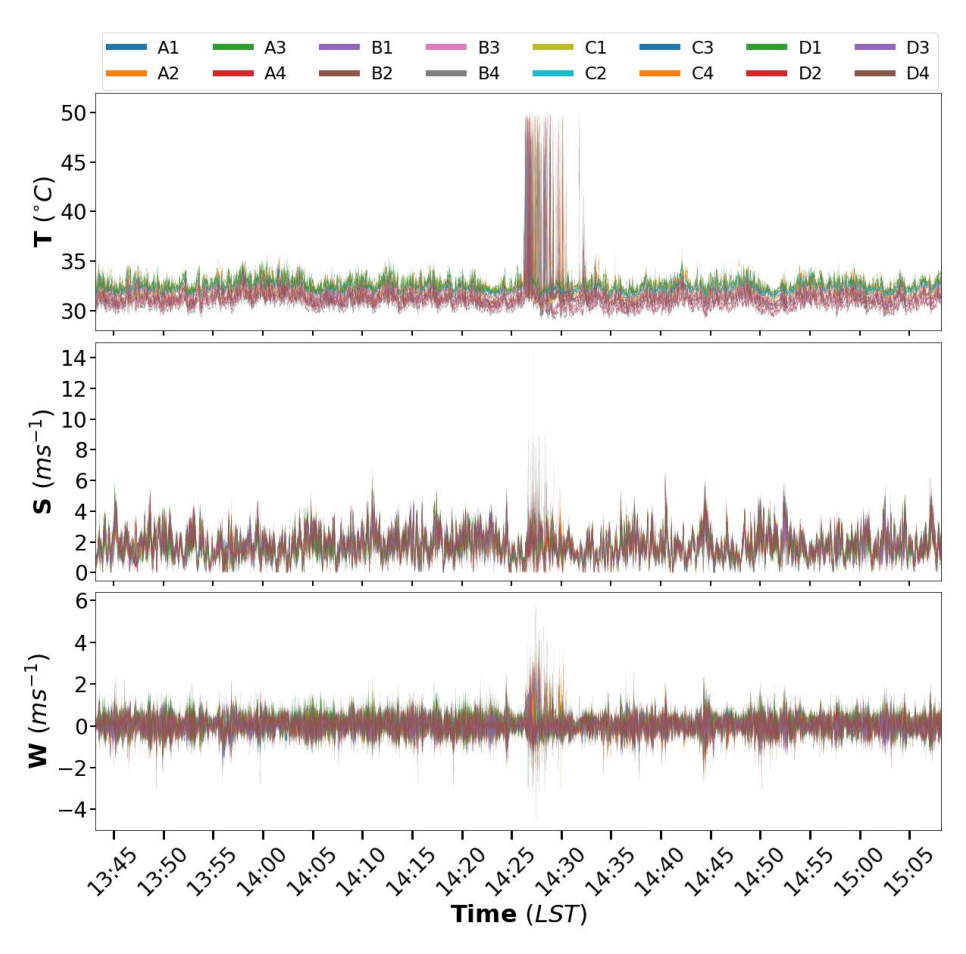


Figure 4. Time series of 10-Hz observations of temperature (T), horizontal wind speed (S) and vertical wind speed (w) observed by the 16 sonic anemometers.

observational period was divided into three periods representing pre-burn, burn and post-burn, which are described in details below.

Figure 4 shows time series of 10 Hz temperature (T), horizontal wind speed (S), and vertical wind speed (w) measured by all 16 sonic anemometers. Note that the sonic temperatures are limited to 50 °C, which is the operational range for the instruments beyond which data are deemed unreliable. Based on the time series and the time when fire was ignited along the western boundary (14:25 LST), the 10-min period from 14:15:13 through 14:25:12 LST is defined as the pre-burn period over which the mean values for u, v, S (horizontal wind speed), w, and T are calculated, and these values are used for calculating perturbations for the pre-burn, burn and post-burn periods. The definition of the burn period, however, is complicated by the fact that the fire front reaches/leaves each sonic anemometer at a different time and consequently the true burn period across the plot varies somewhat depending on the location of each sonic anemometer.

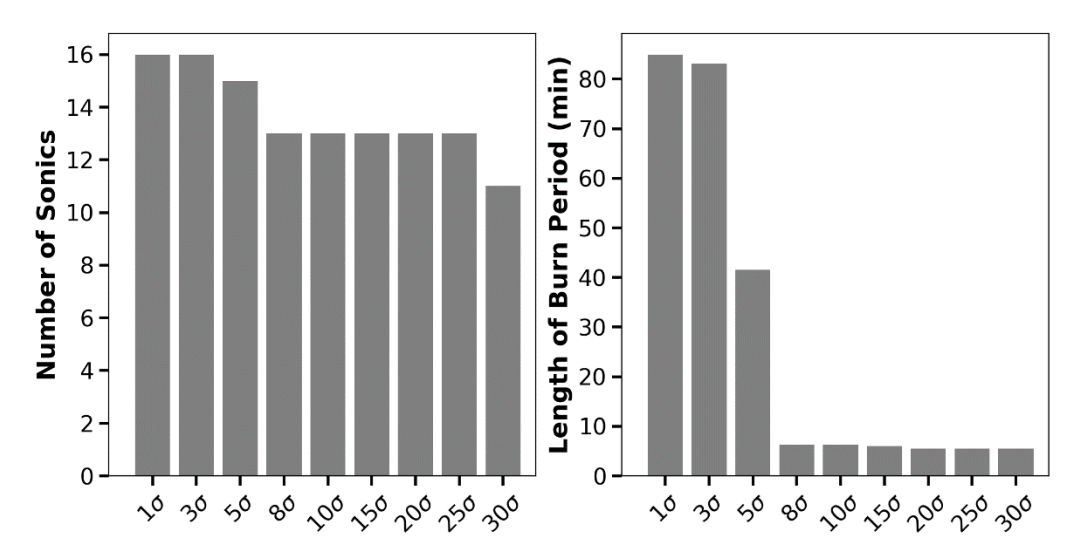


Figure 5. The number of sonic anemometers that recorded temperatures at or above a given threshold value (left) and the length of period over which the threshold was reached or exceeded (right).

Also shown in Figure 4, is the arrival of the fire front at each sonic anemometer, which is marked by a sharp increase in temperature. However, the amount of temperature increase and the rate of increase are not the same across all the sonic anemometers. To create a robust definition of the burn period that can be applied to all the instruments in the 4 x 4 sonic anemometer grid, and eventually to other burns, different temperature thresholds are evaluated. The results of this evaluation are shown in Figure 5.

The increases in sonic temperatures by the fire are measured using integer (n) multiples of the standard deviation (denoted using  $\sigma$ ) of the average temperature over the pre-burn period, where *n* was varied from 1 to 35. Figure 5 shows the number of sonic anemometers whose temperatures exceeded each threshold and the length of the period over which the threshold was exceeded. As the threshold value increases from  $1\sigma$  to  $8\sigma$ , the number of sonic anemometers drops from 16 to 13 and the period drops sharply from just under 60 min to about 6 min. Continued increases in the threshold values from  $8\sigma$  to  $25\sigma$  result in no change in the number of anemometers and very little change in the length of the period (less than 1 min). This analysis suggests that 8 $\sigma$  can be used as the threshold for temperature increases under the influence of the fire. Thresholds lower than 80 would imply a burn period of 30 to 60 min long that, according to Figure 4, would include periods of no fire and therefore de-emphasize the effects of fire in resulting analyses. Applying this criterion to all the sonic anemometers and defining the burn period as between the first and last sonic temperature at or above the threshold leads to the selection of the burn period as 14:26:13 to 14:32:29 LST. Finally, the 10 min following the burn period (14:32:30 to 14:42:29 LST) is defined as the post-burn period.

Following the establishment of the three periods, perturbations are calculated using equations (1) and (2), where the pre-burn averaged values are used as means for the burn and

post-burn periods. Strictly speaking, the perturbations calculated for the burn and post-burn periods are not classical turbulent perturbations; to differentiate the features from classical turbulence, they should be interpreted as being primarily fire-induced turbulent perturbations.

As noted above, horizontal wind velocity is rotated into a streamwise coordinate where the x-component (streamwise component, u) is defined as the prevailing wind direction and the y-component (cross-stream component, v) is defined as perpendicular to and pointing to the left of the prevailing wind. The prevailing wind direction for the rotation is determined by the 10-min pre-burn period average of wind directions across all 16 sonic anemometers. As shown in Figure 6, the average wind directions during the pre-burn period vary slightly across the 16 sonic anemometers, with mean and median wind directions of 225 and 226 degrees, respectively. Thus, 226 degrees is used as the prevailing wind direction for the purpose of coordinate rotation.

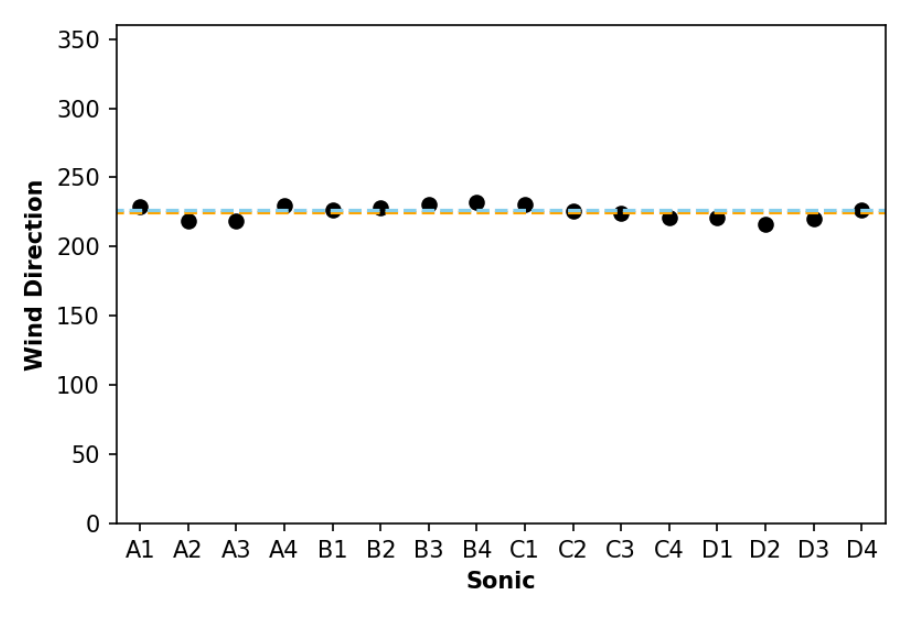


Figure 6. Average wind direction during the pre-burn period for each of the 16 sonic anemometers (dots). The light blue dashed line indicates the average across all 16 sonic anemometers and the orange dashed line denotes the median.

As stated earlier, the primary goal of this study is to understand the impact of fire on the turbulent heat and momentum transfer between the fuel bed and the atmosphere. This goal is

achieved through comparisons of the turbulence properties during the burn period with those of pre-burn and post-burn periods.

For the analysis of turbulent heat and momentum flux, a quadrant analysis technique (Katul *et al.*, 1997, 2006; Heilman *et al.*, 2021) is utilized to delineate the contributions to the turbulent transfer from different types of processes. Specifically, turbulent fluxes are partitioned into four quadrants depending on the sign of the individual perturbation components. For turbulent heat flux,  $\overline{T'w'}$ , the quadrant analysis partitions the flux into ejection (Quadrant 1,  $\overline{T'w'} > 0$ , T' > 0, w' > 0), sweep (Quadrant 3,  $\overline{T'w'} < 0$ , T' < 0, w' < 0), inward interaction (Quadrant 2,  $\overline{T'w'} < 0$ , T' > 0, w' < 0) and outward interaction (Quadrant 4,  $\overline{T'w'} < 0$ , T' < 0, w' > 0) events, shown in Figure 7. The quadrant analysis is also known as sweep-ejection analysis (Heilman *et al.*, 2021). Ejection and sweep (Quadrants 1 and 3) events contribute to positive heat flux through the upward transfer of warmer air from below (ejection) or downward transfer of colder air from above (sweep), while inward and outward interactions (Quadrants 2 and 4) contribute to negative heat flux through downward transfer of warmer air from above (inward interaction) or upward transfer of colder air from below (outward interaction). The warmer/colder here is relative to the background (pre-burn) average temperature.

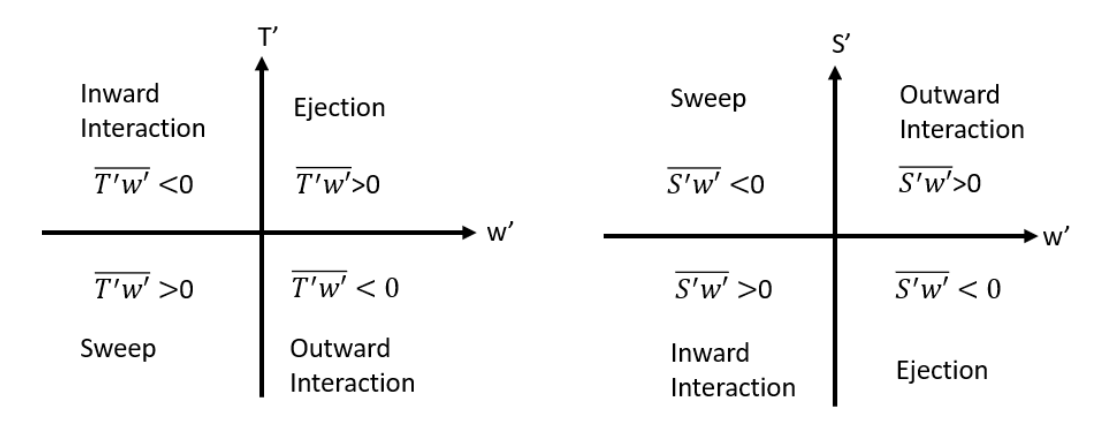


Figure 7. Illustration of sweep-ejection analysis for heat flux (left) and momentum flux (right).

Following Heilman *et al.* (2021), for the quadrant analysis the turbulent momentum flux is estimated using horizontal wind speed perturbations calculated as

$$S' = S - \overline{S} \tag{3}$$

where S denotes horizontal wind speed calculated as

$$S = \sqrt{u^2 + v^2} \tag{4}$$

The momentum flux  $\overline{S'w'}$  sweep-ejection analysis partitions momentum flux into four quadrants that correspond to ejection (Quadrant 4,  $\overline{S'w'}$  < 0, S' < 0, w' > 0), sweep (Quadrant 2,  $\overline{S'w'}$  < 0, S' > 0, w' < 0), inward Interaction (Quadrant 3,  $\overline{S'w'}$  > 0, S' < 0, w' < 0) and outward interaction (Quadrant 1,  $\overline{S'w'}$  > 0, S' > 0, w' > 0) events, shown in Figure 7. Inward interaction and outward interaction events contribute to positive momentum flux through the upward transfer of faster moving air (outward interaction) or the downward transfer of slower moving air (inward interaction), while sweep and ejection events contribute to negative momentum flux through the downward transfer of faster moving air (sweep) or the upward transfer or slower moving air (ejection). The faster/slower is relative to the background (preburn) average wind speed.

#### CHAPTER III - RESULTS AND DISCUSSION

# 3.1 Fire-Induced Perturbations of Wind and Temperature

Figure 8 shows time series of 10-Hz streamwise (u) and cross-stream (v) wind components and perturbation temperatures (T') recorded by all 16 sonic anemometers for this fire. Note that T' is plotted instead of actual temperature to put all three variables on the same plot to help to better visualize the relationships between temperature and wind fluctuations. The natural perturbations, as recorded during the pre-burn period, were small, with magnitudes generally  $< 2.5 \, ^{\circ}C$  for T',  $< 2.5 \, \text{ms}^{-1}$  for u and  $< 1 \, \text{ms}^{-1}$  for v. The fire impinging upon the sonic anemometer is marked by a sharp increase in T', but the magnitude of the temperature increase varies with location, from very little at the sonic anemometers on the western side (labeled 1s) to

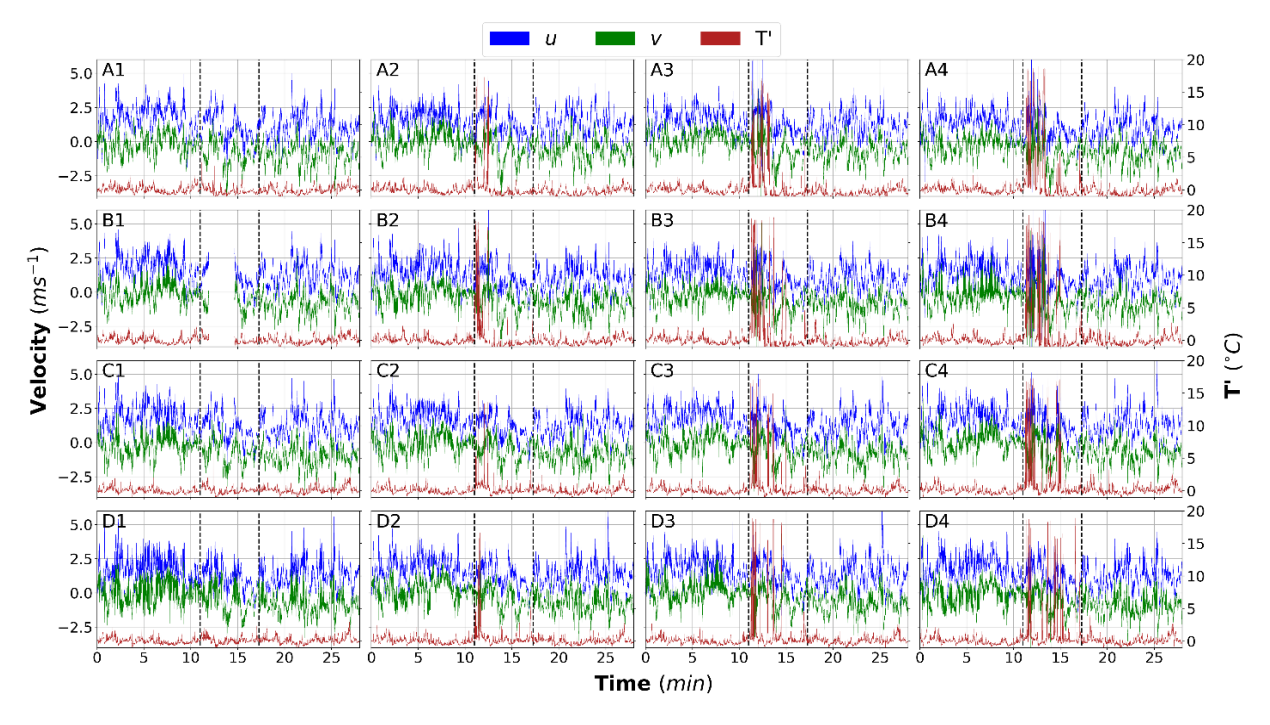


Figure 8. Time series of 10 Hz streamwise (u, blue) and cross-stream (v, green) wind components, and 10 Hz temperature perturbations (T', red) recorded by each sonic anemometer at 2.5 m above the ground. The vertical dashed black lines indicate the burn period determined by the first and last occurrence of when T' is larger than 8 times the standard deviation. Time is the minutes since the start of the pre-burn period.

nearly 20°C the sonic anemometers on the eastern side (labeled 4s). This spatial heterogeneity in T' is consistent with the pattern of the fire spread from the western boundary where it was ignited toward the east and northeast by the southwesterly ambient wind (Figure 4). The fire increases in intensity, as indicated by the sharp rises in T' and the duration of the rise, as it spreads through the burn plot. During the burn period, the u fluctuations decrease somewhat while the v fluctuations increase. The v-component no longer fluctuates around zero, as in the pre-burn period, but rather it is dominated by negative values, indicating a systematic shift in wind direction. There is a tendency for all the variables, particularly u and T', to return towards the pre-burn conditions after the burn, but the v component remains more negative than the pre-burn values.

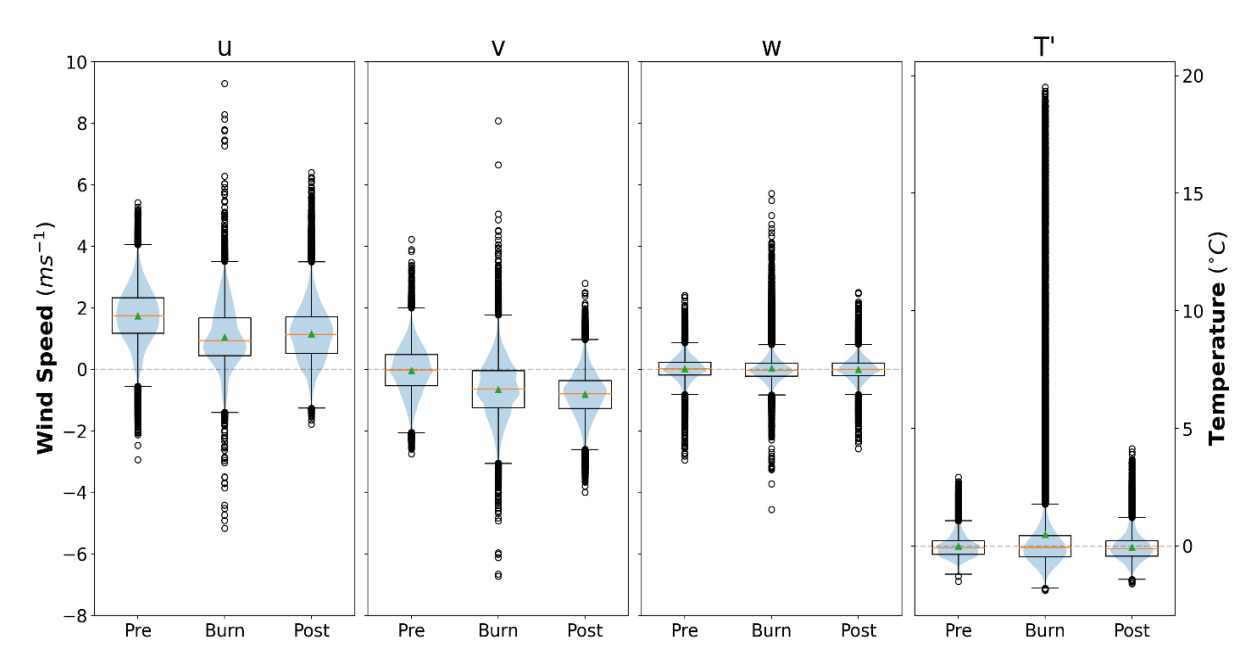


Figure 9. Distributions of 10 Hz streamwise (u), cross-stream (v), and vertical (w) wind components, and temperature perturbations (T') during pre-burn, burn and post-burn periods. The box represents the 25<sup>th</sup> and 75<sup>th</sup> percentile of the data, with data inside the whiskers representing 99.3% of the data. The orange line in the boxes is the median value, the green triangle is the mean, and the blue shading is the density of values.

The observed changes in the distribution of wind and temperature values associated with the fire at all 16 sonics are summarized by the box-whisker plots in Figure 9. The distribution of winds in the pre-burn period shows a mean of 1.7 m s<sup>-1</sup> for u and -0.04 m s<sup>-1</sup> for v, which is expected due to the coordinate rotation into the streamwise direction. The vertical wind, w, also has a mean near zero during the pre-burn period, which confirms that the sonic anemometers were well-leveled. During the burn period, the mean of u dropped from 1.7 to 1.05 m s<sup>-1</sup> while the mean of v changes from -0.04 to -0.65 m s<sup>-1</sup>, indicating an overall shift in wind direction from southwesterly to west-southwesterly. This change in the horizontal wind components is consistent with air being drawn towards the fire and contributing to convergence at the fire front. There is also a fire-induced widening of the distributions of the horizontal wind components, particularly the v component, and an increase in the number and magnitude of outliers to nearly double the pre-burn maximum/minimum values. The large negative values in v during the burn period reinforce the suggestion of convergence in the vicinity of the fire.

Interestingly, there is little evident change in the overall distribution of w during the burn period, except that more and larger outliers are indicated. This result suggests that the fire perturbations are not strongly and persistently affecting w at the height where the sonic anemometers were mounted (2.5 m above the ground). However, since maximum updrafts/downdrafts during the burn period reach speeds of nearly 6 m s<sup>-1</sup> and -5 m s<sup>-1</sup> respectively, which is roughly double those of the pre- and post-burn periods, it is evident that intermittent turbulent eddies associated with the fire more strongly impact w during the burn period. The T' distribution also widens substantially during the burn period ( $\sigma$ =4.24 °C) compared to the pre-burn period ( $\sigma$ =0.48 °C) with the maximum temperature perturbation reaching nearly 20 °C.

The influence of the fire on the horizontal wind components continues into the post-burn period, as the post-burn distributions of u and v fall between those of the pre-burn and burn periods. In contrast, the post-burn w distribution returns to a distribution very close to that of the pre-burn period. Similarly, the T' distribution during the post-burn period is very similar to that of the pre-burn period. The similarities between the w and T' distributions suggest that the two variables are closely related to each other, with large updrafts during the burn period being generated primarily by heating. This result suggests that the fire exhibits behavior more consistent with a buoyant plume than mechanically forced rising motion resulting from converging surface air.

# 3.2 Intensity of Fire-Induced Turbulence

The intensity of fire-induced turbulence can be determined by comparing turbulent kinetic energy (TKE) during the burn and pre-burn period. TKE is defined as the summation of the velocity variance

$$TKE = \left(\overline{u'^2} + \overline{v'^2} + \overline{w'^2}\right)/2 \tag{5}$$

Figure 10 shows time series of 1-minute averaged TKE and the three individual components of the velocity variance for each of the sonic anemometers. The time series indicate lower TKE values in the pre-burn period, larger values during the burn period, and values remaining high but with larger fluctuations in the post-burn period. The burn period TKE is primarily driven by an increase in horizontal velocity variance,  $\overline{u'^2}$  and  $\overline{v'^2}$ , with a pronounced increase in cross-stream component  $\overline{v'^2}$  that is most evident in the northernmost sonic anemometers (A1, A2, A3, and A4). That the horizontal velocity variance,  $\overline{u'^2}$  and  $\overline{v'^2}$ , are

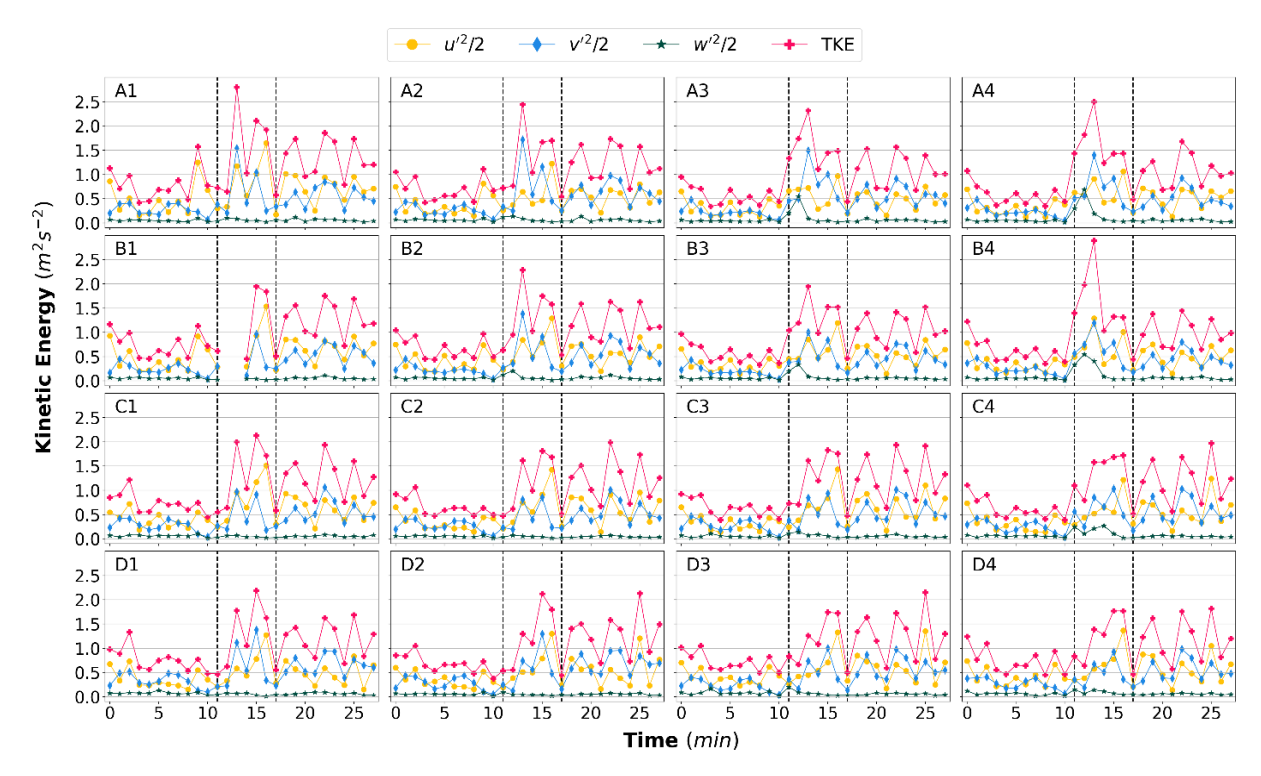


Figure 10. 1-minute averaged turbulent kinetic energy (TKE) (red line) and the three components that make up the TKE for each sonic anemometer. The u component ( $u^{2/2}$ ), v component ( $v^{2/2}$ ), and w component ( $w^{2/2}$ ) are notated as yellow, blue, and dark green, respectively.

larger than the vertical velocity variance,  $\overline{w'^2}$ , at all times suggests that the TKE during this fire was generally dominated by horizontal flow fluctuations. During the burn period, most of the sonic anemometers on the plot experienced two large TKE spikes. For the sonic anemometers in the northeastern corner (A3, A4, B3, and B4), the first TKE increase is accompanied by an increase in  $\overline{w'^2}$ , but an increase in  $\overline{w'^2}$  does not occur during the second TKE spike.

The box-whisker plots in Figure 11 depict the fire-induced changes to the distribution of turbulence intensity as observed by all 16 sonic anemometers. Averaging across all the instruments, the burn period mean TKE is  $1.25 \text{ m}^2\text{s}^{-2}$ , which is roughly double the pre-burn mean of  $0.697 \text{ m}^2\text{s}^{-2}$ . The interquartile range of the burn period TKE was nearly three times the pre-burn period range. The post-burn period does not return to the pre-burn TKE value and remains elevated throughout the ten-minute period  $(1.21 \text{ m}^2\text{s}^{-2})$ . While the  $\overline{w'^2}$  returns to the pre-burn

conditions, the horizontal components remain elevated with  $\overline{u'^2}$  averaging 0.588 m<sup>2</sup>s<sup>-2</sup> and  $\overline{v'^2}$  averaging 0.570 m<sup>2</sup>s<sup>-2</sup>.

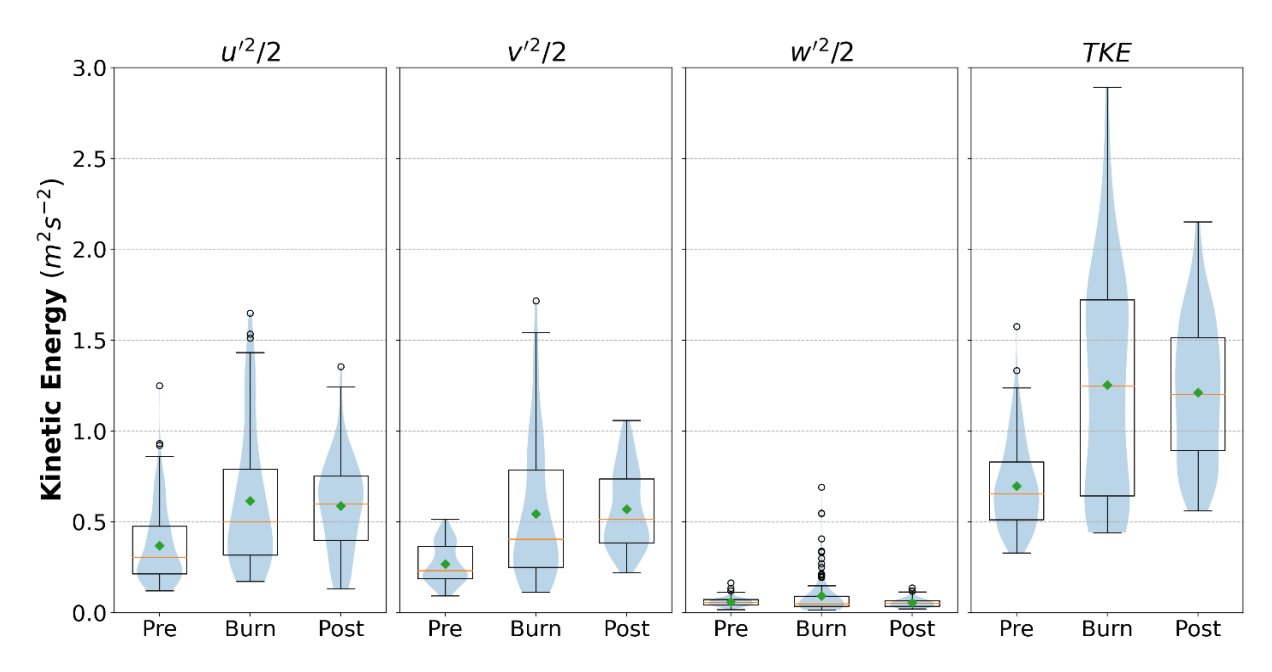


Figure 11. Boxplot distributions of turbulent kinetic energy (TKE) and the velocity variance components ( $u^{2/2}$ ,  $v^{2/2}$  and  $w^{2/2}$ ) during the pre-burn, burn and post-burn periods. The blue shading indicates the distribution, green diamond is the mean value, and orange line is the median.

More specifically,  $\overline{u'^2}$  and  $\overline{v'^2}$  make up 52.9% and 21.4% of the average pre-burn TKE, respectively. During the burn period,  $\overline{u'^2}$  decreased to 49.4% and  $\overline{v'^2}$  increased to 43.5%. As noted earlier (Figures 8 and 9), the burn period also experiences a larger range of horizontal and vertical wind components, which is consistent with the larger range of TKE values in Figure 11.

In the post-burn period, the vertical velocity variance returns to the pre-burn distribution. However, the range of values in the horizontal components are smaller post-burn than during the burn period, but still larger than during the pre-burn period. The medians of the horizontal TKE components are higher in the post-burn period than in either of the other periods, while the  $\overline{u'^2}$  outliers (above the 99.3rd percentile) decrease and the  $\overline{v'^2}$  outliers increase in magnitude. As was

previously discussed, post-burn average wind directions differ from the pre-burn, accompanied by increases in the magnitude of the horizontal winds (Figures 8 and 9). This result is consistent with elevated TKE values persisting into the period after the end of the fire.

Additional analysis of the three components enables an assessment of turbulence anisotropy. Anisotropy is assessed numerically by calculating an anisotropy ratio, which is defined as  $\overline{w'^2}$  divided by 2xTKE. When this ratio approaches 1/3 for a given time period, the period can be said to experience an isotropic turbulent regime (Heilman et al., 2015). The mean  $\overline{w'^2}$  for all the sonic anemometers is 0.0597 m<sup>2</sup>s<sup>-2</sup> for the pre-burn period, 0.0931 m<sup>2</sup>s<sup>-2</sup> for the burn period, and 0.055 m<sup>2</sup>s<sup>-2</sup> for the post-burn period, which yields an anisotropy ratio well below 1/3 at all times. The larger value for the  $\overline{w'^2}$  during the burn period suggests that the fire produces turbulence that is less anisotropic compared to the other periods, but overall the fireinduced TKE is dominated by the horizontal components throughout the observation period. Since the sonic anemometers located on the western and southern sides of the plot show no clear increase in  $\overline{w'^2}$ , the anisotropy ratio is also calculated for each sonic to verify that the mean values did not mask anisotropy variations at individual locations in the burn plot. No individual sonic anemometer reaches a ratio of 1/3, and the highest individual ratio is found at sonic anemometer A4 during the burn period (0.133). This result indicates that overall, the TKE is highly anisotropic and is dominated by the horizontal components for this burn. This result is not surprising as the sonic anemometers are located only 2.5 m above ground where horizontal turbulence dominates over vertical turbulence (Heilman et al., 2015).

## 3.3. Fire-Induced Shear Stress

Turbulent shear stress is commonly measured by shear velocity or friction velocity, defined as

$$u_*^2 = \left(\overline{u'w'}^2 + \overline{v'w'}^2\right)^{\frac{1}{2}} \tag{6}$$

Figure 12 shows time series of 1-minute averages of the friction velocity squared  $(u_*^2)$  and the streamwise  $\overline{u'w'}$  and cross-stream  $\overline{v'w'}$  stress components (also referred to as the kinematic momentum fluxes), observed by each of the sonic anemometers for the three periods. Kinematic momentum fluxes and  $u_*^2$  are generally similar for all the sonic anemometers during the pre-burn period, although three of the northernmost instruments (A2, A3, and A4) indicate a negative spike in  $\overline{u'w'}$  just before the start of the burn period. These spikes contribute to an

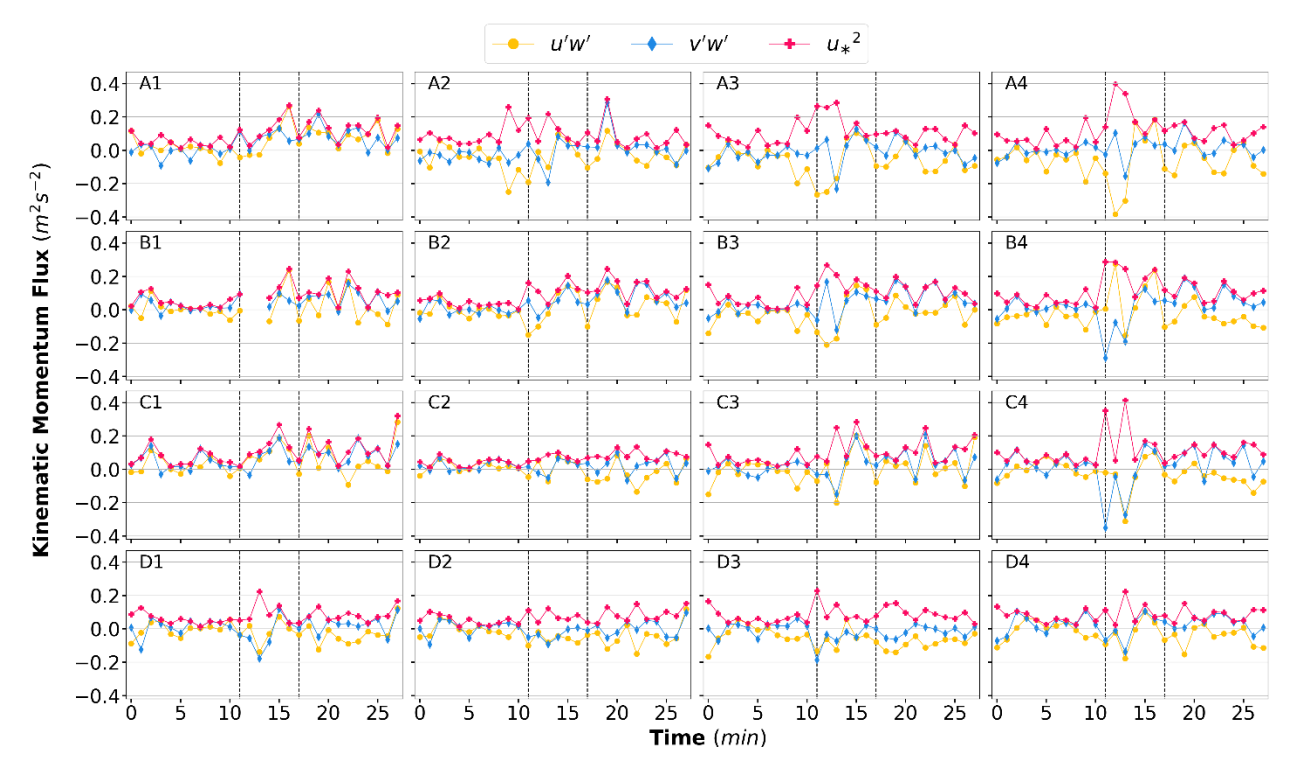


Figure 12. Time series of 1-minute averaged kinematic momentum flux  $(u_*^2)$  and its u- and v-components (u'w') and v'w', separated by sonic anemometer. Yellow circles indicate u'w', blue diamonds indicate v'w', and pink plusses indicate  $u_*^2$ .

increase in  $u_*^2$  at this time as well. It is not clear what caused these features, but candidates include an anomalous burst of wind along the northern edge of the burn plot and contamination of the wind data by activities of the burn managers as they prepared to ignite the fire.

During the burn period,  $u_*^2$  values are largest at the downwind sonic anemometers, with A3, A4, B3, and B4 showing the largest changes compared to the pre-burn period. As  $u_*^2$  values increase in magnitude,  $\overline{u'w'}$  and  $\overline{v'w'}$  vary somewhat across the burn plot during the burn period. In the beginning of the burn period, all the sonic anemometers, besides B4, C1, and C2, experience a negative trend in the  $\overline{u'w'}$ , indicating a downward flux of streamwise momentum. The strongest downward streamwise momentum flux of -0.384 m<sup>2</sup>s<sup>-2</sup> occurs downwind, at the A4 sonic anemometer. Later in the burn period, the streamwise momentum flux turns positive at all but a few sonic anemometers on the south edge of the plot. The fire-induced changes generally increase in magnitude from west (left) to east (right), consistent with the fire-spread pattern. The  $\overline{u'w'}$  values exhibit the largest burn period variation at A4 with  $\sigma = 0.222$  m<sup>2</sup>s<sup>-2</sup>, followed by B4 with  $\sigma = 0.164$  m<sup>2</sup>s<sup>-2</sup>, and similar patterns are observed for  $\overline{v'w'}$ . Overall, variations in  $u_*^2$  suggest an increase in shear stress magnitude in the burn period compared to the pre-burn period, with the easternmost sonic anemometers recording 1-minute averaged increase values that are far greater than the westernmost sonic anemometers.

During the post-burn period, some sonic anemometers (A2, B2, C1, C2, D2) recorded higher  $u_*^2$  than during the burn period, while others (A1, B1, B3, C2, C3, D3) recorded values similar to the burn period. In either case, the average values are larger than during the pre-burn. Sonic A2 shows the largest  $u_*^2$  and  $\overline{v'w'}$  values during the post-burn period (0.309 m<sup>2</sup>s<sup>-2</sup> and 0.117 m<sup>2</sup>s<sup>-2</sup>, respectively), which occur early in the post-burn period. The largest  $\overline{u'w'}$  value

occurs during the last minute of the post-burn at the C1 sonic anemometer (0.283 m<sup>2</sup>s<sup>-2</sup>). Clements et al. (2008) also observed a spike in  $u_*^2$  after the fire front had exited the burn plot of an intense grass fire, which coincided with the time of a dust devil appearing over the plot.

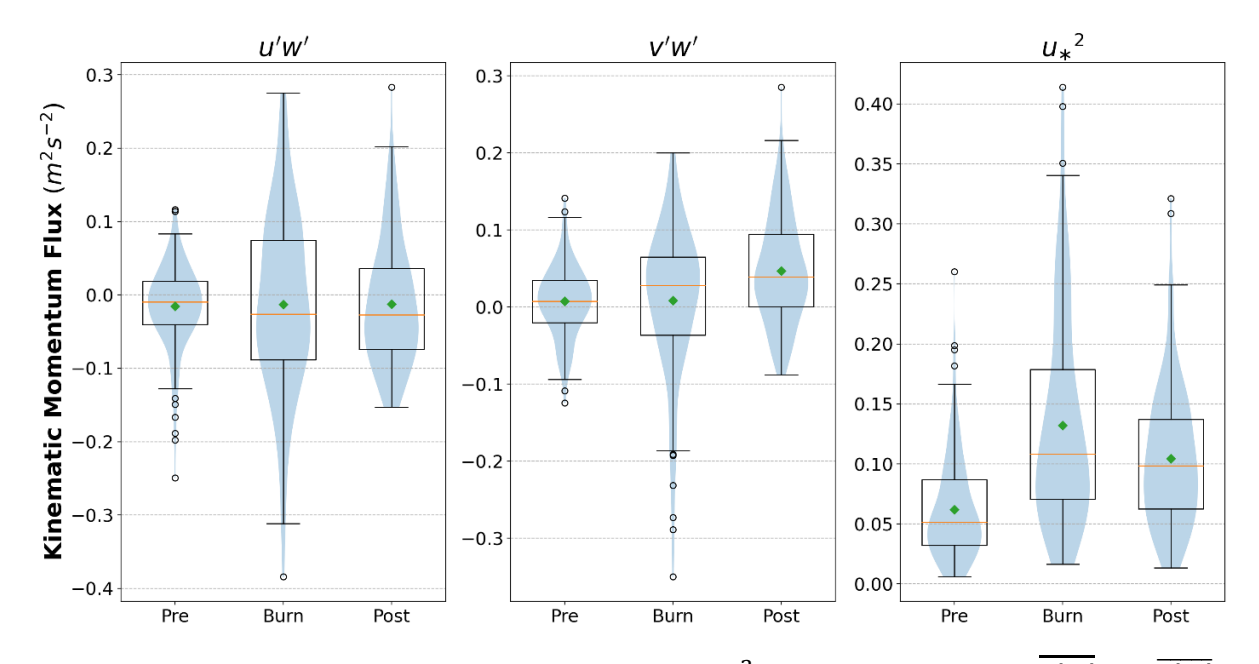


Figure 13. Boxplot distributions of friction velocity  $(u_*^2)$  and its components (u'w') and  $\overline{v'w'}$  during the pre-burn, burn, and post-burn periods. The blue shading indicates the distribution, green diamond is the mean value, and orange line is the median.

The overall distributions of  $u_*^2$ ,  $\overline{u'w'}$ , and  $\overline{v'w'}$  from all 16 sonic anemometers are depicted in Figure 13. During the pre-burn period,  $\overline{u'w'}$  is negative with a mean of -0.015 m<sup>2</sup> s<sup>-2</sup>, indicating the downward transfer of higher momentum air, which is expected when wind speed increases with height. The mean of  $\overline{v'w'}$  is near zero (0.007 m<sup>2</sup> s<sup>-2</sup>), but the spread of the two components is similar, with standard deviations of 0.057 m<sup>2</sup> s<sup>-2</sup> and 0.046 m<sup>2</sup> s<sup>-2</sup>, respectively. The pre-burn stress  $u_*^2$  of 0.061 m<sup>2</sup> s<sup>-2</sup> or friction velocity  $u_*^2$  of 0.25, m s<sup>-1</sup>, are values typically found near the surface during daytime.

Stronger downward (negative)  $\overline{u'w'}$  and upward (positive)  $\overline{v'w'}$  are observed during the fire period, as indicated by more negative (positive) median values for the streamwise (cross-

stream) component, although the mean changes little. The spread is doubled from a standard deviation of 0.046 to 0.098 m<sup>2</sup> s<sup>-2</sup> for  $\overline{u'w'}$  and nearly triple (from 0.05 to 0.124 m<sup>2</sup> s<sup>-2</sup>) for  $\overline{v'w'}$  The stronger upward transfer of cross-stream momentum is consistent with the generation of cross-stream wind and updrafts in the vicinity of the surface fire. Despite this overall fire-induced increase in  $\overline{v'w'}$ , the distribution of the cross-stream momentum is negatively skewed with values of outliers < -0.3, suggesting occasional transfer of higher cross-stream momentum by downdrafts near the vicinity of the fire. Both the mean and standard deviation of the  $u_*^2$  are doubled to 0.13 m<sup>2</sup>s<sup>-2</sup> and 0.086 m<sup>2</sup>s<sup>-2</sup>, respectively, over the pre-burn values. The peak 1-min averaged values of  $u_*^2$  exceed 0.4 m<sup>2</sup>s<sup>-2</sup> (or a friction velocity of 0.6 m s<sup>-1</sup>), which is 2.5 times larger than the pre-burn values. Clements *et al.* (2008) also observed an increase of 3 times in friction velocity in their experiment of high intensity grass fire, although the absolute values of the friction velocity is five times larger (1 and 3 m s<sup>-1</sup> pre fire and during the fire).

Post-burn  $u_*^2$  values are lower than during the burn period but still higher than in the preburn period, driven primarily by the cross-stream component. Values of the  $\overline{v'w'}$  average are more than six times the pre-burn average (0.0471 m<sup>2</sup>s<sup>-2</sup>), with a standard deviation that is between the pre-burn and burn averages (0.069 m<sup>2</sup>s<sup>-2</sup>). The friction velocity therefore does not return to the pre-burn average, although it is lower than the values during the burn period. Other experiments (e.g. Clements *et al*, 2008) noted a return to pre-burn values soon after the passage of the fire, during a period when smoldering was occurring. The results of this analysis suggest that friction velocities do not quickly return to pre-burn values on all fires.

## 3.4 Fire-Induced Turbulent Heat Flux

Time series of 1-minute average turbulence sensible heat flux  $\overline{w'T'}$  for each sonic anemometer are shown in Figure 14 for the three periods, which also shows the overall distribution of heat fluxes for all the sonic anemometers. In the pre-burn period, the sonic anemometers recorded background  $\overline{w'T'}$  values of that averaged around  $5.25 \cdot 10^{-2} Kms^{-1}$  (52.7 Wm<sup>-2</sup>), with a standard deviation of  $3.41 \ 10^{-2} Kms^{-1}$  (34 Wm<sup>-2</sup>). During the burn period, a fire-induced increase in  $\overline{w'T'}$  is evident at all but the westernmost sonic anemometers (A1, B1, C1, and D1), with larger increases appearing at the easternmost instruments. The largest peak  $\overline{w'T'}$  values generally occur early in the burn period, with the A4 sonic having the largest 1-minute averaged  $\overline{w'T'}$  of  $2.13 \ Kms^{-1}$  ( $2.138 \ kWm^{-2}$ ). Based on the IR imaging (Figure 3), after the first three minutes of the burn period there is a slight shift in the burn direction towards the

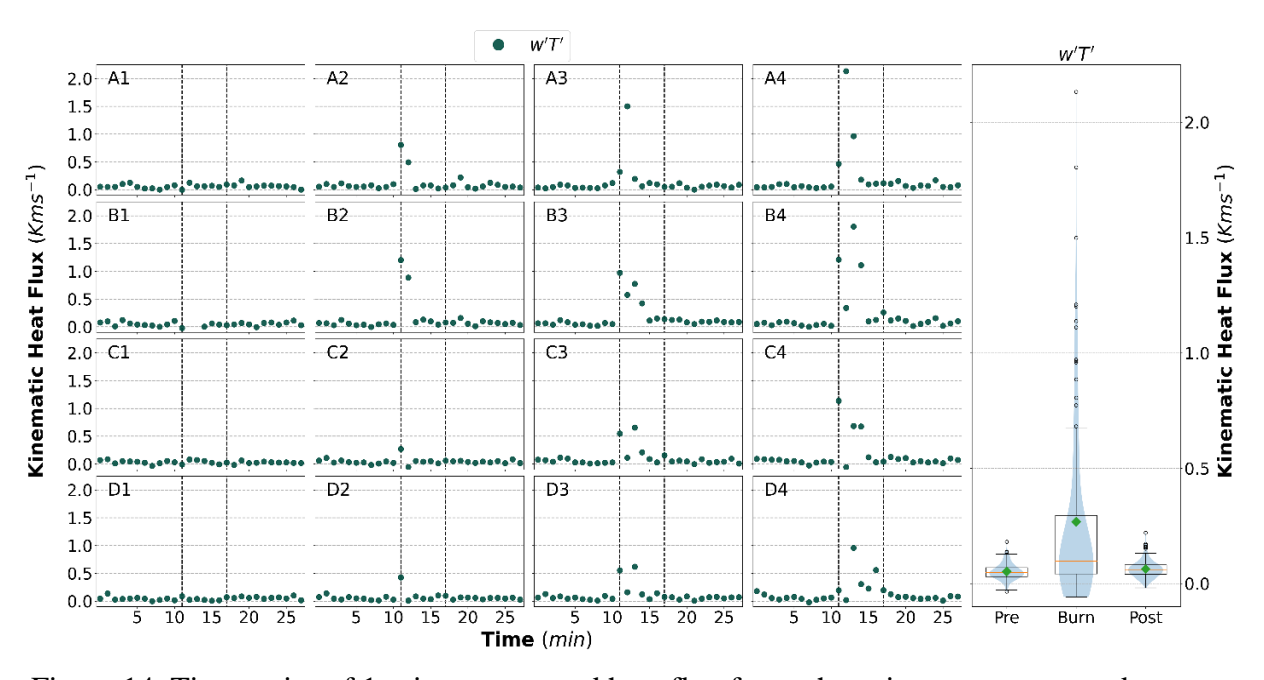


Figure 14. Time series of 1-minute averaged heat flux for each sonic anemometer and an overall distribution of values for all the sonic anemometers. Dark green dots on the 4x4 grid indicate the average heat flux value for each minute. The right panel shows the distribution of the heat flux for the entire burn plot in the pre-burn, burn, and post-burn periods.

southeastern side of the plot. This shift in direction is apparent in the time series for the D4 sonic anemometer, which is located on the southeastern corner of the burn plot, where elevated  $\overline{w'T'}$  values are recorded late in the burn period, at a time when most of the other instruments measured values near zero. The overall distribution of the burn-period  $\overline{w'T'}$  is skewed by larger values since the plot mean was 0.268 Kms<sup>-1</sup> (269 Wm<sup>-2</sup>) but the median was just 0.0974 Kms<sup>-1</sup> (98 W m<sup>-2</sup>).

Values of  $\overline{w'T'}$  during the post-burn period quickly drop back to just slightly above the pre-burn values, with a mean of  $6.35 \cdot 10^{-2} Kms^{-1}$  (64 Wm<sup>-2</sup>) and a standard deviation of  $3.76 \cdot 10^{-2} Kms^{-1}$  (38 Wm<sup>-2</sup>). However, the post-burn period contains several outliers (above the 99.3% percentile), indicating the influence of smoldering on some of the sonic anemometers even after the fire has exited the burn plot. A specific example of the smoldering effect is the D4 sonic anemometer, where the post-burn  $\overline{w'T'}$  (0.126 Kms<sup>-1</sup> or 126 W m<sup>-2</sup>) is about twice the preburn value. The overall modest increase of  $\overline{w'T'}$  in the post-burn period compared to the pre-burn period was also observed in the two wildland fire experiments described in Heilman *et al.* (2019).

# 3.5 Quadrant Analysis of Fire-Induced Turbulent Heat and Momentum Fluxes

A comparison of turbulent heat and momentum fluxes between the pre-burn and the burn periods enables a quantitative assessment of fire-induced changes to the total fluxes. However, it fails to reveal the processes responsible for the changes. In other words, what types of heat or momentum transfer events are mostly affected by the fire? The quadrant analysis (also known as sweep-ejection analysis) described earlier (Figure 7) is applied to the observed turbulent fluxes to provide additional insight into how the fire changes the composition of heat and momentum fluxes. By partitioning the total heat and momentum fluxes into four quadrants representing different types of flux events, the quadrant or sweep-ejection analysis allows for the delineation of the fire influence on specific types of turbulent heat and momentum transfer processes.

Figure 15 shows the magnitude and frequency of heat flux events, including their relative contribution to the total heat flux, observed by each of the 16 sonic anemometers. During the pre-burn period, the partitioning among the four types of events (see Figure 7) by magnitude and frequency exhibits little variation across the 16 sonic anemometers. At all locations, the frequency of turbulent heat flux events is split between ejection and sweep events, with the latter being slightly larger. Together, sweep and ejection account for more than 60% of the total events. The rest is split between outward interaction and inward interaction events, with the former slightly outnumbering (20-23%) the latter (14-19%). A similar partitioning is observed for the heat flux magnitude, but despite being slightly less frequent, the ejection events contribute more to the heat flux than do the sweep events. This apparent inconsistency between the partitioning of the event frequency and the event contribution suggests that ejection events likely involve larger eddies and stronger heat transfer compared to sweep events. This result

during the pre-burn period is comparable to previous ambient daytime measurements observed in other studies (e.g., Heilman *et al.*, 2021).

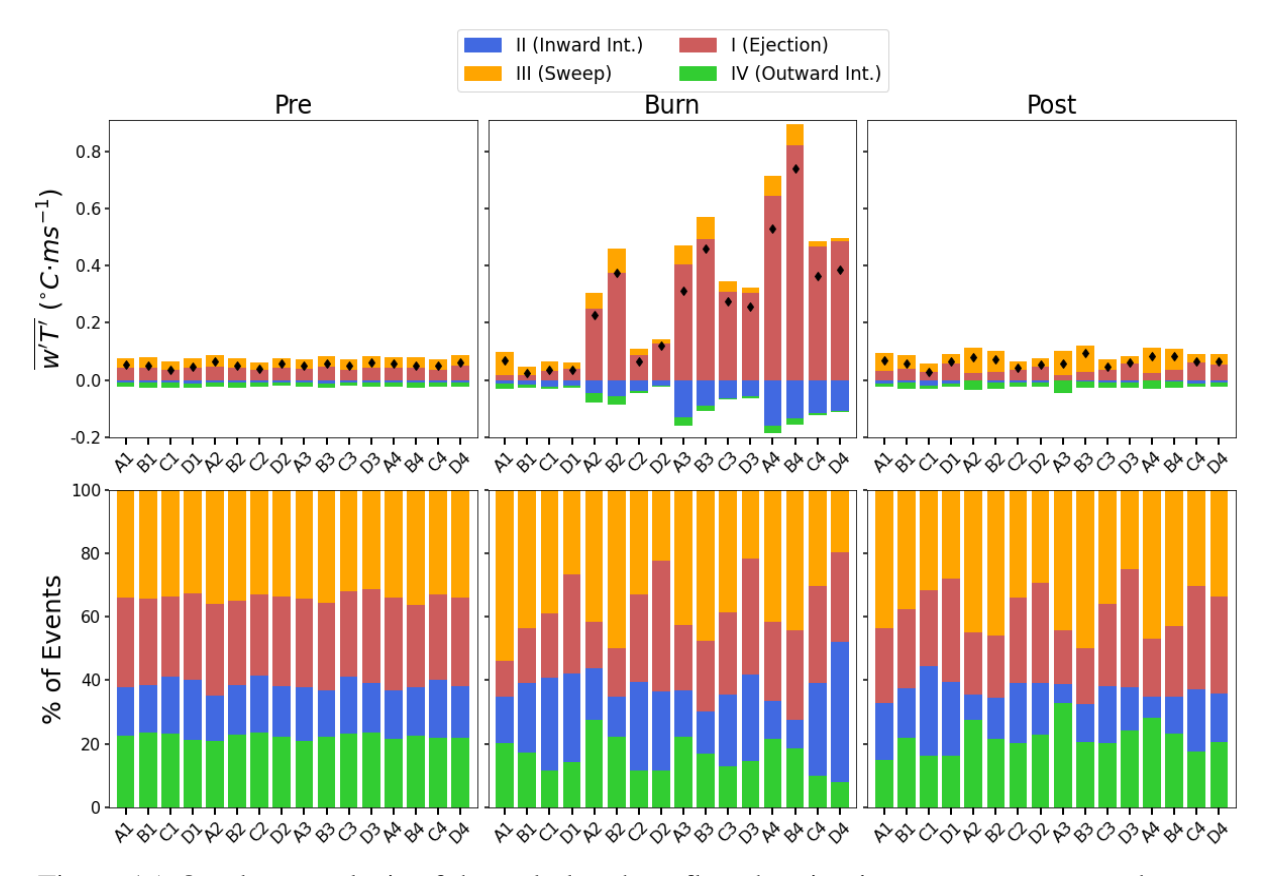


Figure 15. Quadrant analysis of the turbulent heat flux showing instantaneous outward interaction (green), ejection (red), inward interaction (blue), and sweep (orange) events at each of the 16 sonic anemometers, separated by burn period. The top row is the total magnitude of the 10Hz observations for the corresponding T'w' perturbations in each period with the total heat flux value represented as a black diamond. The bottom row is the percentage of events occurring at each sonic separated by burn period. The sonic anemometers are arranged from west to east roughly following the fire spread under the fire plot.

The burn period is marked by substantial heterogeneity across the 16 sonic anemometers. Despite differences in the magnitude of the heat fluxes amongst the anemometers, the increased total heat flux by the fire can be largely attributed to increases in contributions from ejection events, which represent the upward transfer of warmer air from the combustion zone to the atmosphere above. There is also an increase in the inward interaction events, which represent

the downward transfer of warmer air from the atmosphere to the combustion zone. The percentage of the total heat fluxes associated with the sweep and outward interaction events show little change or a slight decrease from the pre-burn to the burn periods, which suggests that the turbulent heat transfer processes represented by these types of events, namely downward transfer of colder air from above to the surface or upward transfer of colder air from the combustion zone to the atmosphere, are not very sensitive to the presence of low-intensity fuel-bed-scale surface fire.

Compared to the magnitude partitioning, the fire-induced changes to the frequency partitioning are less clear. In general, the sonic anemometers that show an increase in the contribution by the inward interaction also exhibit an increase in the frequency of the inward interaction events from the pre-burn to the burn periods. However, an increased contribution by the ejection events does not correspond to an increase in the frequency of the ejection events. There appears to be a match between increased sweep events and increased sweep contribution at several sonics (A2-A4 and B2-B4), although the sweep contribution is overwhelmed by that of ejection at these sonic anemometers.

A key finding from this heat flux sweep-ejection analysis is that turbulent heat fluxes during the burn period are overwhelmingly dominated by ejection events, but there is usually a small or no increase in the frequency of ejection events. This suggests that the presence of a low-intensity fuel-bed-scale fire does not necessarily produce more upward turbulent heat transfer events, but rather that it produces stronger events that quickly transfer and diffuse the sensible heat generated by combustion into the ambient atmosphere above.

During the post-burn period, most sonic anemometers show heat flux values that are smaller than the burn period but still larger than the pre-burn period. The largest contribution to

heat flux magnitudes most often is from sweep events, accompanied also by an increase in the frequency of the events, indicating the occurrence of many events where cold air is transferred downward. The post-burn period also exhibits an increase in the magnitude of outward interaction events, which are associated with the downward transfer of warm air. Similar to the burn period, there is higher variance across all the sonic anemometers for inward interaction events both in magnitude and number of events, depending on burn plot location

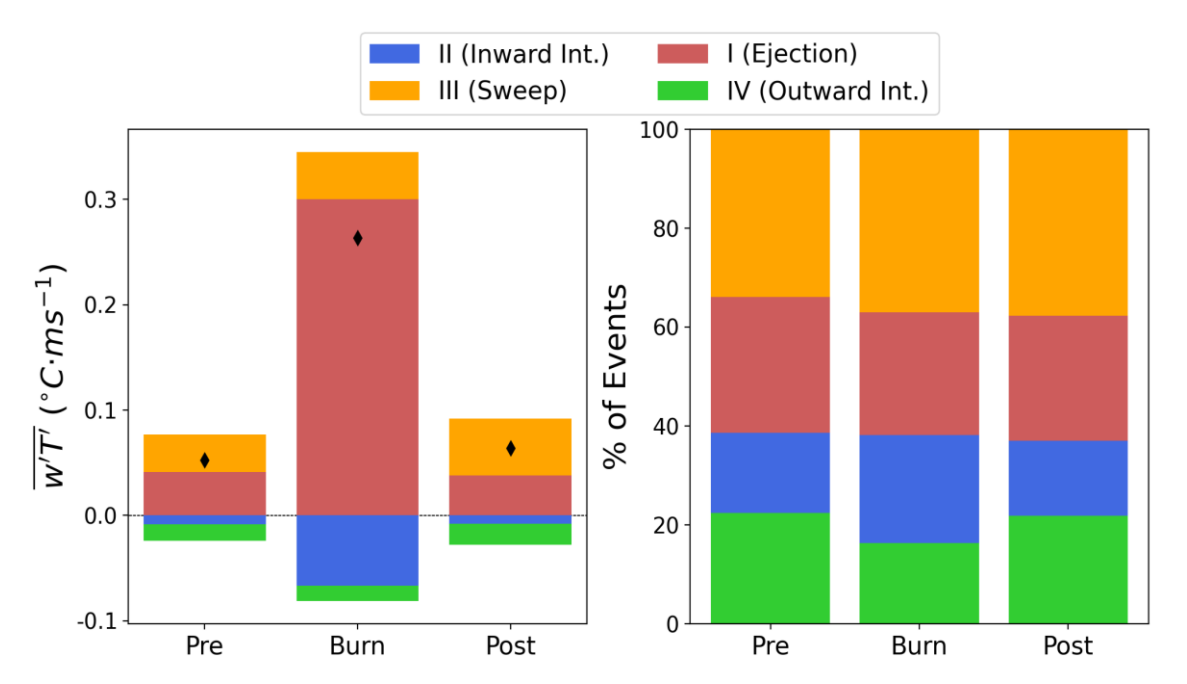


Figure 16. Quadrant analysis of turbulent heat flux events for all sonic anemometers using instantaneous outward interaction (green), ejection (red), inward interaction (blue), and sweep (orange) for each period. The left plot is the summation of the magnitude of events of combined sonic anemometers before, during, and after the burn period. The right plot is the percentage of the type of events before, during, and after the burn.

Figure 16 shows the partitioning of both the frequency and the magnitude of turbulent heat fluxes using data from all 16 sonic anemometers, which shows more clearly how the fire modifies the overall heat flux regime. Similar to the individual sonic heat flux quadrant analysis, the combined heat flux for the pre-burn period is dominated by sweep (33.9%) and ejection (27.5%) events. Inward interactions occur with the lowest overall frequency (16.3%), with

outward interactions occurring 22.4% of the time. This frequency of outward interaction events in the pre-burn period differs somewhat from previous experiments described in Heilman *et al.* (2021) where they were found to occur <20% of the time in the pre-burn period at all levels measured. The magnitude of sweep and ejection events combined makes up 76% of the total heat flux magnitude, while outward interactions and inward interaction contributions are 8.3% and 15.7%, respectively. The dominance of sweep and ejection events in the pre-burn period follows observations made in previous studies (Heilman *et al.*, 2021).

During the burn period, total heat flux magnitudes are more than 2.5 times the pre-burn values. The numbers of each type of event in the burn period are similar to the pre-burn period, with changes smaller than 7% compared to the pre-burn period for all types of events. Previous fire experiments reported an increase in sweep events and a generally proportional decrease in ejection events (Heilman *et al.*, 2021). This fire exhibits a similar change in sweep and ejection events, but the magnitude of the changes is small, likely due to the lower fire intensity compared to fires in previous studies. Additionally, modest changes in the relative frequency of event types for this fire could be a byproduct of combining data from sonic anemometers that were not strongly affected by the fire front (i.e. the westernmost instruments) with instruments that experienced more substantial temperature and horizontal wind perturbations.

The large changes in the magnitude of heat flux events during the burn period suggest that this fire has greater impacts on the magnitude of turbulent heat fluxes than on the frequency of the types of events. Specifically, ejection events dominate the total heat flux in the burn period, making up 70.4% of the total magnitude while sweep and outward interaction events decrease by a third and a sixth, respectively, compared to their contributions during the pre-burn

period. The magnitude of the contribution from inward interaction events increases slightly but is quite similar to the contribution during the pre-burn period.

Heat flux events in the post-burn period more closely resemble the pre-burn period than the burn period, but the magnitude and distribution of events do not entirely return to pre-burn values. As noted in the analyses of TKE and kinematic heat flux (Figures 11 and 13), this result is consistent with smoldering occurring in the burn plot during the post-burn period. The frequency of sweep events exhibits the largest differences (+3.8% of pre-burn and +0.7% of burn period). The magnitudes of post-burn events return to the pre-burn conditions with the exception of sweep events, which remain 1.5 times higher than pre-burn period and 1.3 times higher than the burn period. Outward interaction magnitudes during the post-burn period increased slightly from the pre-burn magnitudes. The magnitude of ejection and inward interactions in the postburn period decreases slightly from the pre-burn period. The changes in the magnitude of events in the post-burn period indicate that this period is still dominated by sweep event magnitudes (37.7%), with ejection event magnitudes, although lower than pre-burn values, still constitute 25.3% of the magnitude of events. Inward interaction event magnitudes slightly decrease with outward interactions increasing slightly compared to the pre-burn magnitudes. This result differs somewhat from the Heilman et al. (2021) results in that they reported both sweep and ejection events returning to pre-burn values, while only the ejections return to pre-burn values for this fire.

Figure 17 shows the decomposition of the kinematic horizontal momentum fluxes  $\overline{w'S'}$  into the four quadrants for each of the 16 sonic anemometers. Compared to the heat fluxes, there is greater variability in the momentum flux magnitudes between the burn periods and within each

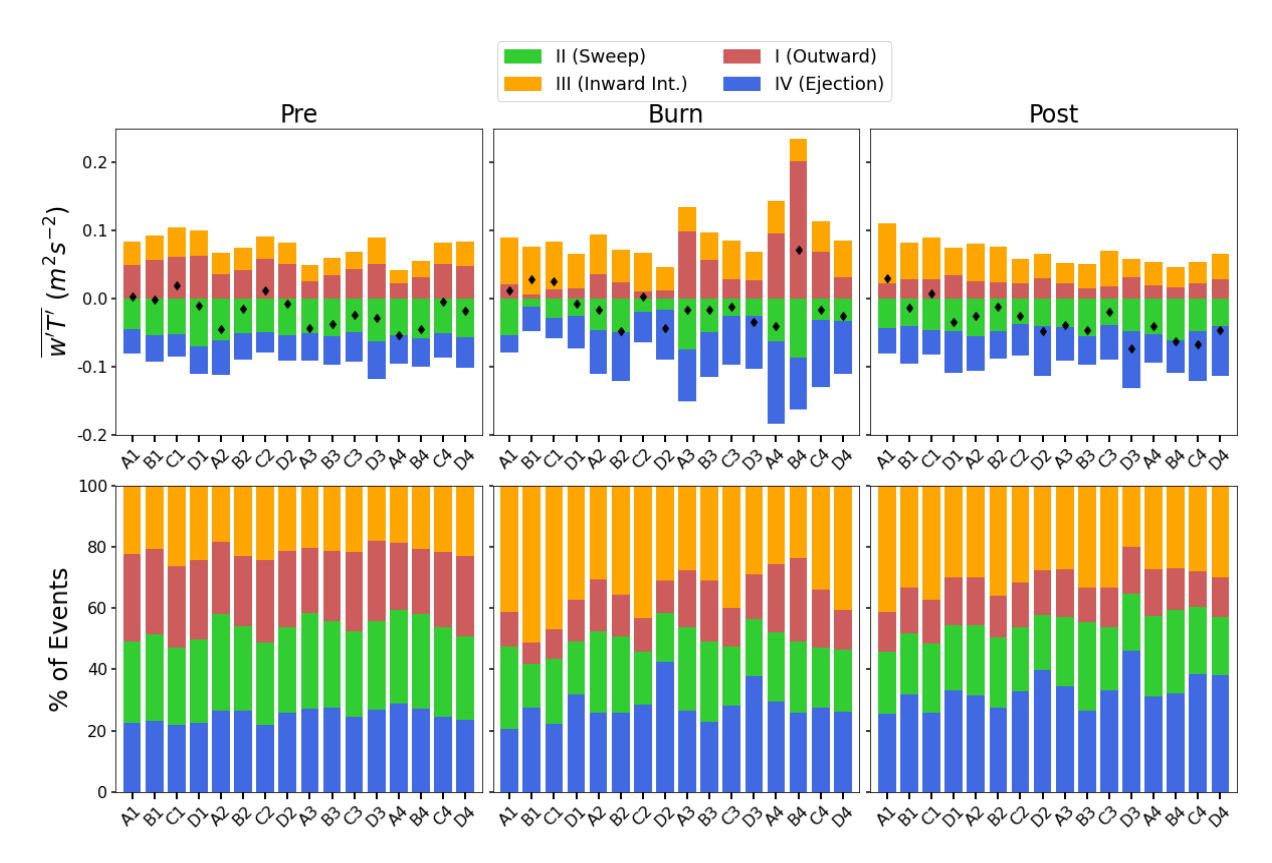


Figure 17. Quadrant analysis of the turbulent kinematic horizontal momentum flux showing instantaneous outward interaction (red), sweep (green), inward interaction (orange), and ejection (blue) events at each of the 16 sonic anemometers, separated by burn period. The top row is the total magnitude of the 10Hz observations for the corresponding *S'w'* perturbations in each period with the total momentum flux value represented as a black diamond. The bottom row is the percentage of events occurring at each sonic separated by burn period. The sonic anemometers are arranged from west to east roughly following the fire spread under the fire plot.

burn period. During the pre-burn period, the total kinematic momentum fluxes, which is a summation of events over all four quadrants, are negative at all but three sonic anemometers. Between the two types of events that make up the negative momentum fluxes, the sweep events (downward transfer of higher horizontal momentum air from the atmosphere to the fuel bed) dominate over the ejection events (upward transfer of lower horizontal momentum air from the fuel bed to the atmosphere above), which is consistent with the more frequent occurrence of sweep events than ejection events. Between the two types of events that contribute to positive

momentum fluxes, the outward interaction events (upward transfer of higher horizontal momentum air from the fuel bed to the atmosphere above) dominate the inward interaction events (downward transfer of lower horizontal momentum air from the atmosphere to the fuel bed), although they occur at similar frequencies.

The changes from the pre-burn to the burn period vary substantially across the sonic anemometer sites. At most sonic anemometer sites, the sign of the total momentum fluxes remains unchanged. Across the anemometer array, the frequency and contribution nearly double for the inward interaction events. The ejection events also exhibit an increase in frequency and contribution at most of the sonic anemometer sites. There is a general decrease in the frequency of sweep and outward interaction events, but the contributions are not consistent, with some sonic anemometers showing increase while others experiencing a decrease in contribution.

An exception to the above general observations between pre-burn and burn period is B4, where the momentum flux changes from a large negative to a large positive value. This change is mainly driven by the large contributions from outward interaction events at this site, which are more than 5 times the magnitude of the pre-fire period. The amount of increase in the contribution from the outward interaction events does not match the small increase (approximately 10%) in the frequency of the events, suggesting strong upward transfer of higher horizontal momentum air associated with large, energetic eddies.

The large heterogeneity in the magnitude of the momentum flux and its composition across the sonic anemometer array during the burn period dissipated substantially into the post-burn period. The magnitude and frequency distributions once again become less dependent on the locations of the sonic anemometers. Despite this tendency to return to the pre-burn distribution, the post-burn period experiences larger contributions and higher frequency from

ejection and inward interaction events than sweep and outward interaction events, which is opposite to the pre-burn period and similar to the burn period.

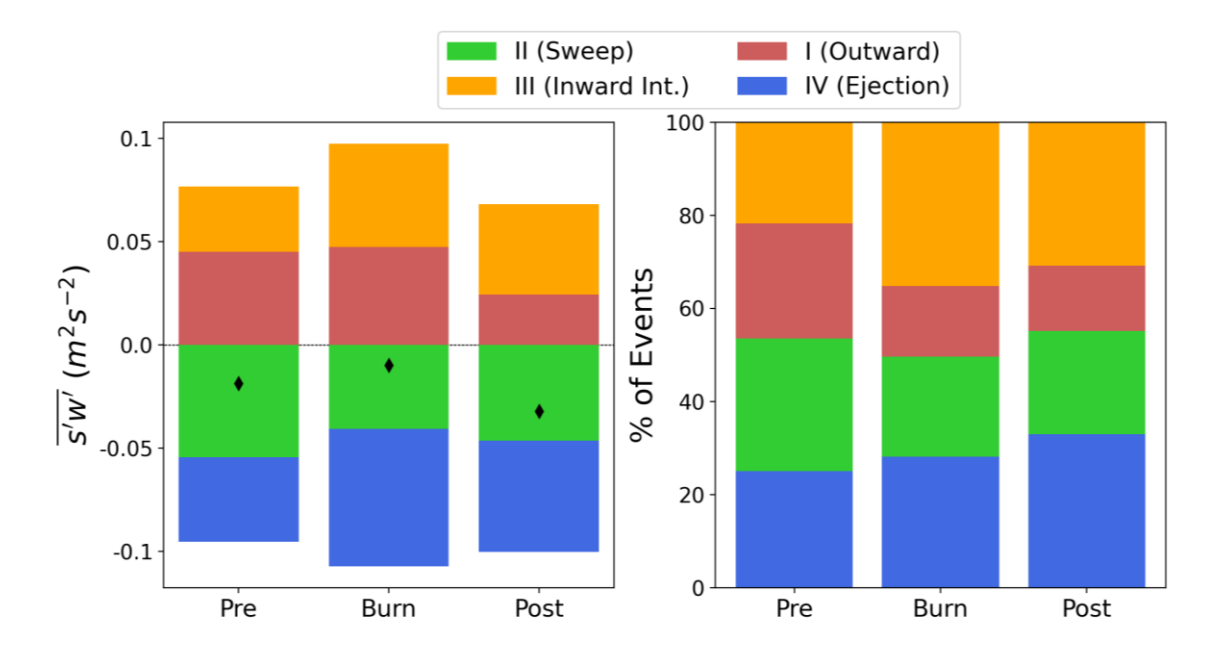


Figure 18. Quadrant analysis of kinematic momentum flux events for all sonic anemometers using instantaneous outward interaction (red), sweep (green), inward interaction (orange), and ejection (blue) for each period. The left plot is the summation of the magnitude of events of combined sonic anemometers before, during, and after the burn period. The right plot is the percentage of the type of events before, during, and after the burn.

Figure 18 shows a quadrant analysis that combines data from all the anemometers, which allows for an assessment of how the fire modified the momentum flux turbulence regime for the whole burn plot. Overall, sweep (31.9%) and outward interaction (26.6%) events dominate the momentum flux magnitudes in the pre-burn period. The increase in the inward and ejection events from the pre-burn to the burn periods makes the contribution more balanced across the four quadrants, suggesting that momentum transfer processes during the burn period are overall less anisotropic than the pre-burn period. In the post-fire period, inward interaction events contribute more to the total magnitude (25.7%) than during the pre-fire period (18.1%), which again suggests that smoldering during the post-fire period strongly affects momentum fluxes. The distribution of events in the combined analysis echoes the results from the individual sonics,

with the pre-burn period showing similar values for all four quadrants, a sharp increase in inward interaction events and decrease in outward events during the burn period, and inward interaction events in the post-burn period that are less numerous than during the burn period but more numerous than during the pre-burn period.

The results of quadrant analysis of momentum fluxes presented above are somewhat different from those of previous studies. Heilman *et al.* (2021) showed that during an intense grass fire and two low-intensity forest understory fires, the magnitude contribution and frequency of sweep and outward interactions events make up more than 60% of the total events, with sweeps being the largest. Whereas in the small fuel-bed scale burn here, inward interactions occur most frequently, followed by ejection events, and together they make up 63% of the total events in the burn period. However, the magnitudes of ejection contributions are larger (32.3%) with inward interactions (24.2%) more similar to outward interaction (23.4%) magnitudes. Deviation of increased inward interaction events and magnitudes compared to previous burns is further observed in the post-burn period.

The frequency of events and magnitude contributions of the post-burn period also differ with increased ejection and inward interactions events, 32.8% and 20.6%, while the burns in Heilman *et al.* (2021) measured a returned close to pre-fire period observations, with sweep and ejection events making up the majority of events and magnitude contributions. In this study, the magnitudes of the post-period saw elevated sweep, inward interaction, and ejections contributions at the expense of outward interaction magnitudes when compared to the pre-burn period.

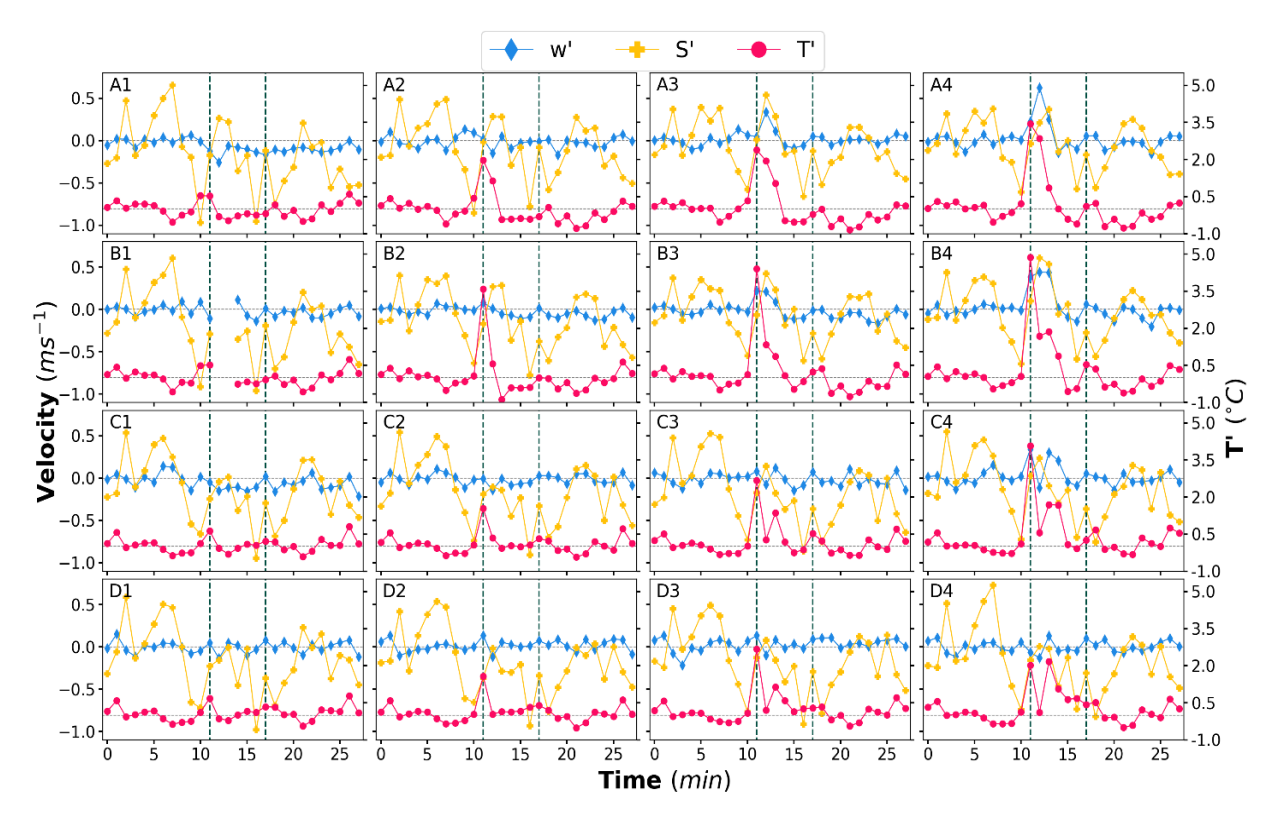


Figure 19. 1-minute averaged perturbations of vertical wind (w') in blue, horizontal wind speed (S') in yellow, and temperature (T') in red. The burn period is represented by the two dark green dashed vertical lines.

To further investigate this departure in momentum flux sweep-ejection results from those reported in Heilman *et al.* (2021), the one-minute time averages of the vertical wind (*w'*), horizontal wind (*S'*), and temperature (T') perturbations are plotted in Figure 19. The time series show that the magnitude of S' variations are similar in the pre-burn, burn, and post-burn periods at all the locations, while the magnitude of variations in w' and T' exhibit more variability from location to location and from pre-burn to burn to post-burn periods. Sonic anemometers on the western side of the burn plot generally experience less variability in w' and T' than those on the eastern side. Additionally, instruments on the western side of the burn plot generally show larger w' and T' perturbations during the burn period than during the pre-burn period. In the post-burn period, w' and T' variations are generally larger than during the pre-fire period, with the most

pronounced differences occurring at the westernmost sonic anemometers. Variations in S' became negative during the burn period and continue into the post-burn period. With S' trending negative for both burn and post-burn periods, it is anticipated that the inward interactions and ejections events would be more frequent and contribute more to the momentum flux in these periods, as seen in Figures 17 and 18. Heilman *et al.* (2021) does not show the speed perturbation and vertical velocity perturbation, making it impossible to explain the apparent difference in the momentum flux sweep-ejection analysis results.

#### CHAPTER IV - CONCLUSION AND FUTURE WORK

This study presents observations of wind and temperature perturbations collected during a fuel-bed scale (10 m x 10 m) prescribed fire experiment conducted on the Silas Little Experimental Forest in New Jersey, USA. This experimental fire was part of a research project sponsored by SERDP. An array of 4 x 4 sonic anemometers, along with a number of other instruments, were deployed to the burn plot to capture fire, fuel, and atmospheric conditions that occurred before, during, and after the burn. The wind and temperature data analyzed in this study were collected from 16 sonic anemometers deployed in a 4 x 4 grid 2.5 m above the ground and that collected data at 10 Hz. The density of turbulence measurements presented here is much greater than that was presented in previously published fire experiments, which enables a deeper analysis of heterogeneities as fire spread across the burn plot than was previously possible. The analysis focuses on assessments of the impact of fire on turbulence characteristics including turbulent intensity, as measured by TKE, turbulent shear stress or the kinematic turbulent momentum flux, as measured by friction velocity, and kinematic turbulent heat flux.

The impacts of the low-intensity surface fire on the surrounding atmosphere are indicated by horizontal convergence at the fire front, as indicated by a general decrease in the streamwise velocity and an increase in the cross-stream velocity, an increase in temperature by as much as 20 °C, and an updraft and downdraft as strong as 6 ms<sup>-1</sup> (-5 ms<sup>-1</sup>). The observed fire exhibits behavior more consistent with a buoyant plume than mechanically forced rising motion resulting from converging surface air. The influence of the fire on horizontal velocity components persists longer after fire front passage while the influence on vertical velocity subsides rapidly behind the fire front.

Fire enhances the intensity of surface layer turbulence, with TKE values 2-3 time higher than the ambient environment. The increase in TKE is attributable to the increase in cross-stream velocity variance and, to a lesser degree, the vertical velocity and streamwise velocity variance. Despite the increase in the vertical velocity variance during the fire, its contribution to TKE is still less than 1/3, indicating that surface-layer turbulence regime remains anisotropic above the combustion zone.

Fire enhances upward sensible heat fluxes substantially by as much as 40 times the flux in the ambient atmosphere (from 50 W m<sup>-2</sup> to 2 kW m<sup>-2</sup>). This change of the sensible heat flux is largely attributable to an increased contribution of upward transfer by turbulent eddies of warmer air from the combustion zone to the atmosphere above, which is also known as ejection events for turbulent heat transfer. However, there is only small or no increase in the frequency of ejection events, which suggests that the presence of a low-intensity fuel-bed-scale fire does not necessarily produce more upward turbulent heat transfer events, but rather strong events associated with large, energetic eddies. The warmer air brought up by the ejection events can also be transferred downward by so-called inward interaction events, which also increased slightly during the fire.

Compared to the heat flux, the impact of the fire on turbulent momentum flux or shear stress is less pronounced. In general, an increase in momentum fluxes is observed during the burn, with friction velocity, a measure of total shear stress on horizontal wind, 2-3 times the ambient value (from ~ 0.25 ms<sup>-1</sup> to 0.6 ms<sup>-1</sup>). Previous studies of grass or forest understory fires also found a three-fold increase in friction velocity despite the much higher absolute values of friction velocity in the previous studies (Heilman *et al.*, 2021). The fire is accompanied by an increase in the downward transfer of lower horizontal momentum air, also known as inward

interaction events, along with a smaller increase in the upward transfer of lower horizontal momentum air referred to as ejection events for momentum transfer. This finding differs from previous observations of a forest understory fire where an increase in sweep (downward transfer of higher horizontal momentum air) and outward interaction (upward transfer of higher horizontal momentum air) occurred (Heilman et al. 2021).

Perhaps the most interesting finding from this study is the large variations in the observed fire-induced perturbation across the sonic anemometer array in the burn plot. The anemometers on the western side of the burn plot where fire was ignited depicted very weak or no signal of the fire despite the proximity to the initial fire line. The sonic anemometers in the center or eastern side of the burn depict clear fire signals that reveal similar nature of fire-induced turbulence, but very different magnitude. Considering the size of the burn plot (10m x 10m), this finding suggests that considerable care should be taken when comparing, contrasting, and combining data from multiple fires or from multiple instruments on the same fire to ensure that significant fire signals are not being over- or under-represented in the analyses that inform the conclusions of the studies. This calls to question using numerical simulations from fire-atmosphere simulation models with horizontal grid spacing larger than 10 m. The results presented here suggest that models should use grid spacings of 1-2 m to adequately resolve the heterogeneities and capture fire-atmosphere interactions that are relevant to turbulence.

This study analyzed sonic anemometer data from one burn that was conducted along with 31 additional 10 m x 10 m burns with different fuel and background meteorological conditions. The analyses presented herein can serve as a model for analyzing the other burns, such that the results can be compared with this burn to determine whether the conditions analyzed here are typical or atypical, and to delineate the effect of fuel and ambient atmospheric conditions on fire-

atmosphere interactions. Additionally, the analysis of all the burns can contribute to comparisons with other prescribed fire experiments as well as identifying the range of variations that can occur in low-intensity, sub-canopy prescribed fires with different amounts and types of understory vegetation and different background meteorological conditions.

Future work should include comparisons with similar sonic anemometer data collected during the other SERDP 10 m x 10 m burns, direct comparisons with the published results of other fire experiments, and the reanalysis of 10 Hz sonic anemometer data from other fire experiments using some or all of the methodologies employed here. This process could contribute to the identification and documentation of a series of steps, protocols, standards, and methodologies by which 10 Hz sonic anemometer data collected during fire experiments can be compared and contextualized. Additionally, the data collected from the other instruments deployed the SERDP 10 m x 10 m fire experiments should be included in future analyses. The potential for spectral and co-spectral analysis to provide more insight into changes that are induced by the fire passage should be investigated. Additional investigations with sonic anemometers and other instruments located at other levels above the ground should be undertaken to determine the effect of height above ground level on these results. It would also be useful to test sonic anemometers that have a larger working temperature range so higher temperatures can be measured and treated as valid data points.

Heat and momentum flux analyses can be very sensitive to averaging and how the burn period is defined. Future burns experiments of this scale should set a pre-burn and post-burn period where there are no persons or objects moving around the burn plot to avoid possible non-natural contamination on the data. Because the burn period is chosen to be between the time when the first and the last sonic anemometers have temperatures satisfying the threshold value

(eight standard deviations), the burn period includes minutes after the fire has passed the sonic location, which is likely to yield an underestimation of the fire effect. Similarly, the inclusion of all 16 sonic anemometers in the analysis, including those that registered no fire signal, also may have contributed to an underestimation. In the real world, fire-induced turbulent circulations and the associated turbulent heat and momentum fluxes are likely to be stronger than what was reported here.

Finally, regarding computer codes and data availability, the Python language was used for all analyses and data management, with the NumPy package used for most statistical calculations, Matplotlib visualization package used for figures, and the Pandas package used for data analyses and data manipulation, all of which are open source packaged in the Python environment. The data management code is hosted on software sharing and version control website and service GitHub, on Joseph Seitz's personal GitHub;

https://github.com/JosephSeitz/SERDP-10x10meter-Burn-Cleaner.

**WORKS CITED** 

### **WORKS CITED**

- Abatzoglou, J.T. and Williams, A.P., (2016) Impact of anthropogenic climate change on wildfire across western US forests. *Proceedings of the National Academy of Sciences*, **113**, pp.11770-11775.
- Amaya, M.A., and Clements C.B. (2020) Evolution of plume core structures and turbulence during a wildland fire experiment. *Atmosphere*, **11**, 842.
- Balch, J.K., Bradley, B.A., Abatzoglou, J.T., Nagy, R.C., Fusco, E.J. and Mahood, A.L. (2017) Human-started wildfires expand the fire niche across the United States. *Proceedings of National Academy of Sciences of the United State of America*, **114**, 2946-2951.
- Beals, E.A. (1914) The value of weather forecasts in the problem of protecting forests from fire *Monthly Weather Review*, **42**, 111–119.
- Beer, T. (1993) The speed of a fire front and its dependence on wind speed. *International Journal of Wildland Fire* **3**, 193–202.
- Bennie, J., Huntley, B., Wiltshire, A., Hill, M.O. and Baxter, R. (2008) Slope, aspect and climate: Spatially explicit and implicit models of topographic microclimate in chalk grassland. *Ecological Modeling*, **216**, 47-59.
- Billmire, M., Frenc, N.H.F., Loboda, T., Owen, R.C. and Tyner, M. (2014) Santa Ana winds and predictors of wildfire progression in southern California, *International Journal of Wildland Fire*, **23**, 1119-1129.
- Byram, G.M. (1940) Sun and wind and fuel moisture. *Journal of Forestry*, **38**, 639–640.
- Byram, G.M., (1954) Atmospheric conditions related to blowup fires. Station Paper SE-SP-35. Asheville, NC: USDA-Forest Service. Southeastern Forest Experiment Station. 36 pp.
- Calviño-Cancela, M, Chas-Amil, M.L., García-Martínez, E.D. and Touza, J. (2017) Interacting effects of topography, vegetation, human activities and wildland-urban interfaces on wildfire ignition risk. *Forest Ecology and Management*, **397**, 10-17.
- Carrier, G.F., Fendell, F.E. and Wolff, M.F. (1991) Wind-aided fire spread across arrays of discrete fuel elements. I. Theory. *Combustion Science and Technology*, **75**, pp.31-51.
- Clark, K.L., Heilman, W.E., Skowronski, N.S., Gallagher, M.R., Mueller, E., Hadden, R.M., and Simeoni, A. (2020) Fire behavior, fuel consumption, and turbulence and energy exchange during prescribed fires in pitch pine forests. *Atmosphere*, **11**, 242.
- Clark, T.L., Coen, J., and Latham, D. (2004) Description of a coupled atmosphere-fire model. *International Journal of Wildland Fire*, **13**, 49–63.
- Clark, T.L., Radke, L., Coen, J., and Middleton, D. (1999) Analysis of small-scale convective dynamics in a crown fire using infrared video camera imagery. *Journal of Applied Meteorology*, **38**, 1401–1420.

- Clark, T.L., Jenkins, M.A., Coen, J.L. and Packham, D.R., (1996) A coupled atmosphere-fire model: Role of the convective Froude number and dynamic fingering at the fireline. *International Journal of Wildland Fire*, **6**, pp.177-190.
- Clements, C.B., and Seto, D. (2015) Observations of fire-atmosphere interactions and near-surface heat transport on a slope. *Boundary-Layer Meteorology*, **154**, 409-426.
- Clements, C.B., Kochanski, A.K., Seto, D., Davis, B., Camacho, C., Lareau, N.P., Contezac, J., Restaino, J., Heilman, W.E., Krueger, S.K. and Butler, B. (2019) The FireFlux II experiment: a model-guided field experiment to improve understanding of fire—atmosphere interactions and fire spread. *International Journal of Wildland Fire*, **28**, 308-326.
- Clements, C.B., Kochanski, A.K., Seto, D., Davis, B., Camacho, C., Lareau, N.P., Contezac, J., Restaino, J., Heilman, W.E., Krueger, S.K., Butler, B., Ottmar, R.D., Vihnanek, R., Flynn, J., Filippi, J.B., Barboni, T., Hall, D.E., Mandel, J., Jenkins, M.A., O'Brien, J., Hornsby, B., and Teske, C. (2019) The FireFlux II experiment: a model-guided field experiment to improve understanding of fire–atmosphere interactions and fire spread. *International Journal of Wildland Fire*, **28**, 308-326.
- Clements, C.B., Zhong, S., Bian, X., and Heilman, W.E. (2008) First observations of turbulence generated by grass fires. *Journal of Geophysical Research*, **113**, D22102.
- Clements, C.B., Zhong, S., Bian, X., Heilman, W.E., and Byun, D.W. (2008), First observations of turbulence generated by grass fires. *Journal of Geophysical Research*, **113**, D22102.
- Clements, C.B., Zhong, S., Goodrick, S., Li, J., Potter, B.E., Bian, X., Heilman, W.E., Charney, J.J., Perna, R., Jang, M. and Lee, D. (2007) Observing the dynamics of wildland grass fires: FireFlux—A field validation experiment. *Bulletin of the American Meteorological Society*, **88**, 1369-1382.
- Countryman, C. (1972) The fire environment concept. *USDA Forest Service*. Pacific Southwest Forest and Range Experiment Station, Berkeley, CA. 12p
- Di Virgilio, N., Facini, O., Nocentini, A., Nardino, M., Rossi, F. and Monti, A., (2019) Four-year measurement of net ecosystem gas exchange of switchgrass in a Mediterranean climate after long-term arable land use. *GCB Bioenergy*, **11**, pp.466-482.
- Ebel, B.A. (2013) Simulated unsaturated flow processes after wildfire and interactions with slope aspect. *Water Resources Research*, **49**, 8090-8107
- Finney, M.A., Cohen, J.D., Forthofer, J.M., McAllister, S.S., Golner, M.J., Gorham, D.J., Saito, K., Akafuah, N.K., Adam, B.A., and English, J.D. (2015) Role of buoyant flame dynamics in wildfire spread. *Proceedings of the National Academy of Sciences*, **112**, 9833-9838.
- Forthofer, J.M., and Goodrick, S.L. (2011) Review of vortices in wildland fire. *Journal of Combustion*, **2011**, Article ID 984363.
- Gill, A.M., Stephens, S.L. and Cary, G.J. (2013) The worldwide wildfire problem. *Ecological Applications*, **23**, 438-454.
- Heilman, W.E., (2021) Atmospheric turbulence in wildland fire environments: implications for fire behavior and smoke dispersion. *Fire Management Today.* **79**, pp.24-29.

- Heilman, W.E., Bian, X., Clark, K.L. and Zhong, S. (2019) Observations of turbulent heat and momentum fluxes during wildland fires in forested environments. *Journal of Applied Meteorology and Climatology*, **58**, pp.813-829.
- Heilman, W.E., Bian, X., Clark, K.L., Skowronski, N.S., Hom, J.L. and Gallagher, M.R. (2017) Atmospheric turbulence observations in the vicinity of surface fires in forested environments. *Journal of Applied Meteorology and Climatology*, **56**, 3133-3150.
- Heilman, W.E., Barnerjee, T., Clements, C.B., Clark, K.L., Zhong, S., and Bian X. (2021) Observations of sweep-ejection dynamics for heat and momentum fluxes during wildland fires in forested and grassland environments. *Journal of Applied Meteorology and Climatology*, **60**, 185-199
- Jain, P., Wang, X. and Flannigan, M.D. (2017) Trend analysis of fire season length and extreme fire weather in North America between 1979 and 2015. *International Journal of Wildland* Fire, **26**, 1009-1020.
- Katul, G., Poggi, D., Cava, D., and Finnigan, J. (2006) The relative importance of ejections and sweeps to momentum transfer in the atmospheric boundary layer. *Bound.-Layer Meteor.*, **120**, 367–375.
- Katul, G., Kuhn, G., Schieldge, J., and Hsieh, C.-I. (1997) The ejection sweep character of scalar fluxes in the unstable surface layer. *Bound.-Layer Meteor.*, **83**, 1–26.
- Katurji, M., Zhang, J., Satinsky, A., McNair, H., Schumacher, B., Strand, T., Valencia, A., Finney, M., Pearce, G., Kerr, J. and Seto, D. (2021) Turbulent Thermal Image Velocimetry at the Immediate Fire and Atmospheric Interface. *Journal of Geophysical Research: Atmospheres*, **126**, p.e2021JD035393
- Kitzberger, T., Falk, D.A., Westerling, A.L., and Swetnam T.W. (2017) Direct and indirect climate controls predict heterogeneous early-mid 21st century wildfire burned area across western and boreal North America. *PLOS ONE*, **12**, e0188486.
- Kuwana, K., Sekimoto, K., Saito, K., and Williams, F.A. (2008) Scaling fire whirls. *Fire Safety Journal*, **43**, 252-257.
- Linn, R.R., Goodrick, S.L., Brambilla, S., Brown, M.J., Middleton, R.S., O'Brien, J.J. and Hiers, J.K., (2020) QUIC-fire: A fast-running simulation tool for prescribed fire planning. *Environmental Modelling & Software*, **125**, p.104616.
- Linn, R. R., and Cunningham, P. (2005) Numerical simulations of grass fires using a coupled atmosphere–fire model: Basic fire behavior and dependence on wind speed. *Journal of Geophysical Research*, **110**, D13107.
- Linn, R.R., Goodrick, S.L., Brambilla, S., Brown, M.J., Middleton, R.S., Obrien, J.J, and Heirs, K. (2020) QUIC-Fire: A fast-running simulation tool for prescribed fire planning. *Environmental Modeling and Software*, **125**, 104616
- Littell, J.S., Peterson, D.L., Riley, K.L., Liu, Y. and Luce, C.H. (2016). A review of the relationships between drought and forest fire in the United States. *Global Change Biology*, **22**, 2353-2369.

- Liu, Y., Stanturf, J., and Goodrick, S. (2010) Trends in global wildfire potential in a changing climate. *Forest Ecology and Management*, **259**, 685-697.
- Luo, L., Tang, Y., Zhong, S., Heilman, W.E., and Bian, X. (2013) Will future climate favor large wildfires in the Western United States, *Journal of Applied Meteorology and Climatology*, **52**, 2410-2417.
- Mell, W., Jenkins, M.A., Gould, J., and Cheney, P. (2007) A physics-based approach to modelling grassland fires. *International Journal of Wildland Fire*, **16**, 1–22.
- Mell, W., Maranghides, A., McDermott, R., and Manzello, S.L. (2009) Numerical simulation and experiments of burning douglas fir trees. *Combustion Flame*, **156**, 2023–2041.
- Moreno, J.M., Torres, I., Luna, B., Oechel, W.C., and Keely, J.E. (2013) Changes in fire intensity have carry-over effects on plant responses after the next fire in southern California chaparral. *Journal of Vegetation Science*, **24**, 395-404.
- Potter, B.E. (1996) Atmospheric properties associated with large wildfires. *International Journal of Wildland Fire* **6**, 71–76.
- Potter, B.E. (2012): Atmospheric interactions with wildland fire behavior I: Basic surface interactions, vertical profiles and synoptic structures. *International Journal of Wildland Fire*, **21**, 779-801.
- Povak, N.A., Hessburg, P.F. and Salter, R.B. (2018) Evidence for scale-dependent topographic controls on wildfire spread. *Ecosphere*, **9**(10): e02443.
- Rothermel, R.C. (1972). A mathematical model for predicting fire spread in wildland fuels. USDA Forest Service, Intermountain Forest and Range Experiment Station, Research Paper INT-115. (Ogden, UT)
- Rothermel R.C., and Anderson, H.E. (1966) Fire spread characteristics determined in the laboratory. USDAForest Service, Intermountain Forest and Range Experiment Station, Research Paper INT-30. (Ogden, UT)
- Schmidt, I.T., O'Leary, J.F., Stow, D.A., Uyeda, K.A., and Riggan, P. (2016) Use of ultra-high spatial resolution aerial imagery in the estimation of chaparral wildfire fuel loads. *Environmental Monitoring and Assessment*, **188**, 697.
- Seto D., Clements, C.B., and Heilman, W.E. (2013) Turbulence spectra measured during fire front passage. *Agricultural and Forest Meteorology*, **169**, 195-210.
- Seto, D., Strand, T.M., Clements, C.B., Thistle, H., and Mickler, R. (2014) Wind and plume thermodynamic structures during low-intensity subcanopy fires. *Agricultural and Forest Meteorology*, **198-199**, 53-61.
- Seto, D., and Clements, C.B. (2011) Fire whirl evolution observed during a valley wind-sea breeze reversal. *Journal of Combustion*, 2011.
- Sharples, J.J. (2009) An overview of mountain meteorological effects relevant to fire behaviour and bushfire risk. *International Journal of Wildland Fire* **18**, 737-754.

- Sharples, J.J., McRae, R.H.D., Wilkes, S.R. (2012) Wind–terrain effects on the propagation of wildfires in rugged terrain: Fire channelling. *International Journal of Wildland Fire*, **21**, 282-296.
- Skowronski, N., and Hom, J.L. (2015): Observations of fire-induced turbulence regimes during low-intensity wildland fires in forested environments: Implications for smoke dispersion. *Atmospheric Sciences Letters*, **16**, 453–460.
- Spracklen, D.V., Logan, J.A., Mickley, L.J., Mickley, L.J., Park, R.J., Yevich, R., Westerling, A.L., and Jaffe, D.A. (2007) Wildfires drive interannual variability of organic carbon aerosol in the western U.S. in summer. *Geophysical Research Letters*, **34** (16).
- Stocks, B.J., Alexander, M.E., and Lanoville, R.A. (2004) Overview of the International Crown Fire Modelling Experiment (ICFME). *Canadian Journal of Forest Research*, **34**, 1543-1547.
- Stull, R.B., (1988) An introduction to boundary layer meteorology (Vol. 13). Springer Science & Business Media.
- Sullivan, A.L. (2009a) Wildland surface fire spread modelling, 1990–2007. 1. Physical and quasi-physical models. *International Journal of Wildland Fire*, **18**, 349–368.
- Sullivan, A.L. (2009b) Wildland surface fire spread modelling, 1990–2007. 2. Empirical and quasi-empirical models. *International Journal of Wildland Fire*, **18**, 369–386.
- Sullivan, A.L. (2009c) Wildland surface fire spread modelling, 1990–2007. 3. Simulation and mathematical analogue models. *International Journal of Wildland Fire*, **18**, 387–403.
- Tang, Y., Zhong, S., Luo, L., Bian, X., Heilman, W.E., and Winkler, J. (2015) The potential impact of regional climate change on fire weather in the United States. *Annals of the Association of American Geographers*. **105**, 1-21.
- Taylor, S.W., Wotton, B.M., Alexander, M.E., and Dalrymple, G.N. (2004) Variation in wind and crown fire behaviour in a northern jack pine black spruce forest. *Canadian Journal of Forest Research*, **34**, 1561-1576.
- Viegas, D.X., and Neto, L.P. (1991) Wall shear stress as a parameter to correlate the rate of spread of a wind-induced forest fire. *International Journal of Wildland Fire*, **1**, 177–188.
- C. E. Van Wagner. (1979) A laboratory study of weather effects on the drying rate of jack pine litter. *Canadian Journal of Forest Research*. 9(2): 267-275. https://doi.org/10.1139/x79-044
- Werth, P.A., Potter, B.E., Clements, C.B., Finney, M.A., Goodrick, S.L., Alexander, M.E., Cruz, M.G., Forthofer, J.A., and McAllister, S.S. (2011) Synthesis of knowledge of extreme fire behavior: For fire managers. General Technical Report PNW-GTR-854, US Department of Agriculture, Forest Service, Pacific Northwest Research Station, Vol. I. Portland, OR, 144.
- Wolff, M.F., Carrier, G.F., and Fendell, F.E. (1991) Wind-aided firespread across arrays of discrete fuel elements. II. Experiment. *Combustion Science and Technology*, **77**, 261–289.

Zhong, S., Wang, T., Sciusco, P., Shen, M., Pei, L., Nikolic, J., McKeehan, K., Kashongwe, H., Hatami-Bahman-Beiglou, P., Camacho, K., Akanga, D., Charney, J., and Bian, X. (2021) Will land use land cover change drive atmospheric conditions to become more conducive to wildfires in the United States? *International Journal of Climatology*, **41**, 3578-3597.